

# Low mass X-ray binaries as a stellar mass indicator for the host galaxy

M. Gilfanov

*Max-Planck-Institut für Astrophysik, 85741 Garching b. München, Germany  
Space Research Institute, Moscow, Russia*

20 February 2018

## ABSTRACT

Using results of Chandra observations of old stellar systems in eleven nearby galaxies of various morphological types and the census of LMXBs in the Milky Way, we study the population of low mass X-ray binaries and their relation to the mass of the host galaxy. We show that the azimuthally averaged spatial distribution of the number of LMXBs and, in the majority of cases, of their collective luminosity closely follows that of the near-infrared light. Considering galaxies as a whole, we find that in a broad mass range,  $\log(M_*) \sim 9 - 11.5$ , the total number of LMXBs and their combined luminosity are proportional to the stellar mass of the host galaxy. Within the accuracy of the light-to-mass conversion, we cannot rule out the possibility of a weak dependence of the  $X/M_*$  ratio on morphological type. However, the effect of such a dependence, if any, does not exceed a factor of  $\sim 1.5 - 2$ .

The luminosity distributions of LMXBs observed in different galaxies are similar to each other and, with the possible exception of NGC1553, are consistent with the average luminosity function derived from all data. The average XLF of LMXBs in nearby galaxies has a complex shape and is significantly different from that of HMXBs. It follows a power law with a differential slope of  $\approx 1$  at low luminosities, gradually steepens at  $\log(L_X) \gtrsim 37.0 - 37.5$  and has a rather abrupt cut-off at  $\log(L_X) \sim 39.0 - 39.5$ . This value of the cut-off luminosity is significantly, by an order of magnitude, lower than found for high mass X-ray binaries.

**Key words:** galaxies: fundamental parameters – galaxies: elliptical and lenticular – galaxies: spiral – X-rays: galaxies – X-rays: binaries

## 1 INTRODUCTION

X-ray binaries are known to be an important contributor to the emission of the host galaxy in the X-ray energy domain (see e.g. a recent review by Fabbiano & White 2003). In the absence of an actively accreting supermassive black hole and/or a large amount of hot gas, they account for the major fraction of the host galaxy's X-ray luminosity, as illustrated by the example of the Milky Way. Depending on the mass of the donor star, X-ray binaries are subdivided into low,  $M_{\text{opt}} \lesssim 1 M_\odot$ , and high,  $M_{\text{opt}} \gtrsim 8 M_\odot$ , mass X-ray binaries (LMXB and HMXB respectively) having very different evolutionary time scales. The life time of high mass X-ray binaries is limited by the nuclear time scale of the massive donor star,  $\lesssim 10^6 - 10^7$  years, i.e. is comparable to the duration of a star formation event. The X-ray active phase of a low mass X-ray binary is delayed with respect to formation of the compact object by the nuclear evolution time scale of the donor star and/or binary orbit decay time

scale,  $\sim 10^9 - 10^{10}$  years (Verbunt & van den Heuvel 1995). The duration of the subsequent X-ray active phase can be of the same order or shorter (Podsiadlowski et al. 2002; Pfahl et al. 2002). These numbers define different relations of high and low mass X-ray binaries to the star formation process. In a naive picture, short living HMXBs provide prompt emission during and shortly after the star formation event. The LMXBs ignition/life time exceeds, by several orders of magnitude, the characteristic time scale of a star formation event and might be comparable to the life time of the host galaxy. Consequently, one might expect that their population is defined by the cumulative effect of the star formation episodes experienced by the host galaxy throughout its lifetime, i.e. is proportional to its total stellar mass. Grimm et al. (2002) studied the population of X-ray binaries in the Milky Way and provided a preliminary calibration of the LMXB- $M_*$  and HMXB-SFR relations.

In a more realistic approach, one should consider details of the formation and evolution of X-ray binaries and

**Table 1.** The sample of nearby galaxies – general data

Name	D Mpc (2)	Morph. Type (3)	Photom. Type (4)	$A_e$ arcsec (5)	B–V RC3 (6)	$M_*/L_{\text{NIR}}$ $M_\odot/L_\odot$ (7)	$s_0$ (8)	$m_{\text{tot}}$ (9)	Ref. X-ray (10)
NGC 4472	16.0	-4.7	-7.7	208.0	0.95	0.85	1.07	4.9	a
NGC 4697	10.5	-4.7	-4.4	143.9	0.89	0.77	0.83	6.1	b
NGC 5846	24.0	-4.7	-4.3	125.4	0.96	0.86	1.05	6.4	c
M84	17.0	-4.2	-8.0	101.9	0.94	0.83	1.07	5.9	d
NGC 1553	24.2	-2.3	2.1	131.3	0.87	0.75	0.81	5.8	e
Cen A	3.5	-2.1	10.1	238.9	0.88	0.76	0.52	4.5	f
NGC 1316	18.6	-1.7	-9.9	161.5	0.87	0.75	0.96	5.3	g
NGC 1291	8.9	0.1	-10.2	109.2	0.91	0.80	1.09	5.5	h
M81	3.6	2.4	2.2	396.4	0.82	0.70	0.64	3.8	i
M31	0.8	3.0	5.4	2501.2	0.68	0.56	0.53	0.5	k
M101	7.2	5.9	5.9	688.9	0.44	0.39	0.54	6.9	j

(2) – distance; (3), (4) – Morphological and photometric type (HyperLeda Database, Prugniel & Heraudeau (1998), <http://www-obs.univ-lion1.fr/hypercat>); (5) – B-band circular effective aperture (diameter) (RC3 catalog, de Vaucouleurs et al. 1991); (6) – B–V color index corrected for galactic and internal extinction (RC3 catalog, de Vaucouleurs et al. 1991); (7) – K-band mass-to-light ratio calculated as described in subsection 2.3; (8), (9) – slope and asymptotic total K-band magnitude obtained from the near-infrared growth curve fit as described in subsection 3.2; References for X-ray data: (a) – Maccarone et al. (2003), (b) – Sarazin et al. (2001), (c) – Trinchieri & Goudfrooij (2002), (d) – Finoguenov & Jones (2002), (e) – Blanton et al. (2001), (f) – Kraft et al. (2001), (g) – Kim & Fabbiano (2003), (h) – Irwin et al. (2002), (i) – Swartz et al. (2003), (j) – Kong et al. (2002), (k) – Pence et al. (2001).

take into account a continuous distribution of the masses of the donor stars, which depends on the star formation history of the host galaxy. The X-ray emission from X-ray binaries following a star formation event should be a continuous function of time, dominated by HMXBs at the early times and by LMXBs at the later times (e.g. Ghosh & White 2001) with a possible contribution of intermediate mass X-ray binaries (IMXB) in between (Podsiadlowski et al. 2002; Pfahl et al. 2002). The role of IMXBs in other galaxies is not well studied, neither theoretically nor observationally. In the case of the Milky Way galaxy, the intermediate mass range,  $M_{\text{opt}} \sim 2 - 5 M_\odot$ , is sparsely populated. In addition, a number of effects, such as metallicity variations, shape of the IMF, etc can complicate the picture.

Various correlations between the X-ray and optical/far-infrared properties of galaxies have been noted and studied in the past (e.g. Griffiths & Padovani 1990; David et al. 1992). Although the X-ray data lacked sufficient spatial resolution and adequate energy coverage, David et al. (1992) suggested that the existence of such correlations could be understood in a two component model consisting of an old and young population having different relations to the current star formation activity and stellar content of the galaxy.

The Chandra observatory, thanks to its sub-arcsecond angular resolution, presented for the first time an opportunity to study the population of X-ray binaries in nearby (within  $\lesssim 15 - 20$  Mpc from the Sun) galaxies in a nearly confusion-free regime and to investigate their relation to the fundamental parameters of the host galaxy, such as stellar mass and star formation rate. Optical identifications of the compact sources in the nearby galaxies are (potentially) available only for the most nearby galaxies and there is a limited possibility to distinguish between LMXBs and HMXBs in other galaxies, based on their X-ray emission in the Chandra bandpass. However, in the naive picture, out-

lined above, one might expect, that at high star formation rates, e.g. in young distant star-forming galaxies or in starbursts in merging and interacting galaxies, the population of compact sources is dominated by HMXBs, whereas in old stellar systems, e.g. elliptical galaxies or bulges of spiral galaxies, the primary contribution comes from LMXBs. Quantitatively, one might use the well studied population of X-ray binaries in the Milky Way to approximately calibrate the relative abundance of HMXB and LMXB as a function of the SFR/ $M_*$  ratio (Grimm et al. 2002, 2003).

Based on the Chandra observations of the nearby star forming galaxies and studies of the high mass X-ray binaries in the Milky Way and SMC, Grimm et al. (2003) explored quantitatively the relation between the population of HMXB sources and the current value of the star formation rate in the host galaxy. They found that, in the broad range of the star formation regimes and rates, the X-ray luminosity distribution of HMXBs in  $\log(L_X) \sim 35.5 - 40.5$  luminosity range can be approximately described by a “universal” luminosity function, whose shape is a  $L_X^{-1.6}$  power law with a cut-off at  $\log(L_X) \sim 40.5$  and with a normalization proportional to the star formation rate. They showed that the  $L_X$ –SFR relation between total luminosity of HMXBs and the star formation rate derived for the nearby galaxies holds for distant star forming galaxies at redshifts up to  $\sim 1.3$  in the Hubble Deep Field North.

In the present paper we study the population of LMXBs and its relation to the stellar mass of the host galaxy, using results of Chandra observations of nearby galaxies of various morphological types, ranging from ellipticals to spirals. The structure of the paper is as follows. In section 2 we describe our sample and details of the X-ray and near-infrared data. In particular, in the subsection 2.2 we point out the importance of contamination by the CXB sources and in the subsection 2.5 we discuss the influence of statistical effects

**Table 2.** The sample of nearby galaxies – X-ray and near-infrared data

Name	$a_X$	$L_{\text{NIR}}$	$M_*$	$L_{X,\text{min}}$	$N_X$	$L_X$	$\Delta N_X$	$\Delta L_X$	$N_X/M_*$	$L_X/M_*$	mode
	(2)	(3)	(4)	(5)	(6)	(7)	(8)	(9)	(10)	(11)	(12)
NGC 4472	50–200	18.70	15.82	1.0	$28.7 \pm 5.6$	$87.2^{+11.9}_{-10.2}$	196.0	57.0	$14.2 \pm 2.8$	$9.1^{+1.2}_{-1.1}$	0.97
NGC 4697	30–300	4.87	3.77	1.0	$12.1 \pm 4.0$	$24.2^{+5.2}_{-4.2}$	82.7	24.0	$25.2 \pm 8.3$	$12.8^{+2.7}_{-2.2}$	0.93
NGC 5846	100–300	10.90	9.36	3.0	$4.9 \pm 3.0$	$25.7^{+4.7}_{-3.2}$	153.2	65.7	$16.9 \pm 10.4$	$9.8^{+1.8}_{-1.2}$	0.91
M84	30–200	13.10	10.92	1.0	$19.1 \pm 4.8$	$54.9^{+9.2}_{-7.6}$	130.6	38.0	$13.7 \pm 3.4$	$8.5^{+1.4}_{-1.2}$	0.95
NGC 1553	30–300	43.90	32.94	2.0	$18.8 \pm 5.0$	$125.0^{+15.0}_{-12.3}$	313.0	117.1	$10.1 \pm 2.7$	$7.4^{+0.9}_{-0.7}$	0.97
NGC 1553	30–100	20.50	15.38	2.0	$7.7 \pm 2.9$	$23.8^{+4.1}_{-3.2}$	127.8	47.8	$8.8 \pm 3.3$	$4.7^{+0.8}_{-0.6}$	0.94
Cen A	100–300	1.84	1.40	0.1	$36.6 \pm 6.3$	$16.3^{+5.2}_{-4.0}$	0.0	0.0	$26.1 \pm 4.5$	$11.6^{+3.7}_{-2.8}$	0.89
NGC 1316	30–150	18.60	13.96	1.0	$23.1 \pm 5.0$	$56.0^{+8.6}_{-7.2}$	157.4	45.8	$12.9 \pm 2.8$	$7.3^{+1.1}_{-0.9}$	0.96
NGC 1291	30–200	4.70	3.74	0.3	$27.7 \pm 5.5$	$28.2^{+6.8}_{-5.5}$	39.0	6.9	$17.8 \pm 3.5$	$9.4^{+2.3}_{-1.8}$	0.93
M81	30–200	3.07	2.14	0.1	$22.1 \pm 4.9$	$13.2^{+6.1}_{-3.9}$	0.0	0.0	$10.3 \pm 2.3$	$6.2^{+2.9}_{-1.8}$	0.81
M31	30–500	1.86	1.05	0.1	$19.8 \pm 4.5$	$7.4^{+3.7}_{-2.3}$	0.0	0.0	$18.9 \pm 4.3$	$7.1^{+3.5}_{-2.2}$	0.79
M101	30–120	0.30	0.12	0.1	$3.3 \pm 2.2$	$0.9^{+1.5}_{-0.3}$	0.0	0.0	$27.7 \pm 18.3$	$7.2^{+12.5}_{-2.7}$	0.36
Milky Way	(a)	4.02	2.27	0.1	$15.0 \pm 3.9$	$7.9^{+5.3}_{-2.5}$	0.0	0.0	$6.6 \pm 1.7$	$3.5^{+2.3}_{-1.1}$	0.70

(2) – X-ray aperture (diameter) range used for the source selection, arcsec; (3) – K-band luminosity in the aperture range  $a_X$  specified in the previous column,  $10^{10} L_\odot$ ; (4) – stellar mass in units of  $10^{10} M_\odot$  in the aperture range  $a_X$ , computed from K-band luminosity and infrared mass-to-light ratio (subsection 2.3, Table 1); (5) – lower X-ray luminosity limit used for the source selection,  $10^{38} \text{ erg/s}$ ; (6), (7) – number of sources detected in the aperture range  $a_X$  with luminosity exceeding  $L_{X,\text{min}}$  and their total luminosity in units of  $10^{38} \text{ erg/s}$ ; (8) – number of sources between  $10^{37} \text{ erg/s}$  and lower luminosity limit  $L_{X,\text{min}}$  estimated using the average luminosity function as described in section 5; (9) – the same as (8) but for the total luminosity,  $10^{38} \text{ erg/s}$ ; (10) – ratio of the total number of sources with  $L_X > 10^{37} \text{ erg/s}$  to the stellar mass, sources per  $10^{10} M_\odot$ ; (11) –  $L_X$ –stellar mass ratio,  $10^{38} \text{ erg/s}$  per  $10^{10} M_\odot$ ; (12) – ratio of most probable value of the total luminosity (mode of the probability distribution) to the expectation mean (section 2.5) (a) – using the LMXB sources located at  $X > 0$  and at the projected galactocentric distance of 1–10 kpc (section 3.5); the NIR luminosity was estimated correspondingly, using the NIR growth curve of M31.

on the total luminosity of X-ray binaries in a galaxy. In section 3 we present X-ray and near-infrared growth curves and demonstrate that the spatial distribution of X-ray binaries closely follows that of the near-infrared light. In section 4 we show that the luminosity distributions in different galaxies from our sample have similar shape and derive the average luminosity function of LMXBs. In section 5 we show that the total number of LMXBs and their collective luminosity is proportional to the stellar mass of the host galaxy. In section 6 we discuss various aspects and astrophysical applications of the obtained results as well as peculiar case of NGC1553 and in section 7 we summarize our findings.

## 2 THE SAMPLE

Our sample includes 11 nearby galaxies of various morphological types observed with Chandra. To minimize the contribution of high mass X-ray binaries, we focus our study on old stellar systems – E, S0 galaxies and the bulges of spiral galaxies, typically having negligible star formation activity.<sup>1</sup> The list of galaxies along with their general optical/NIR characteristics is given in Table 1. This sample of external nearby galaxies was complemented by the population of low

mass X-ray binaries in the Milky Way, based on the results of Grimm et al. (2002).

### 2.1 X-ray data

To study the spatial and luminosity distribution of X-ray binaries in 11 external galaxies, we used published lists of X-ray sources detected by Chandra. The references to the original X-ray publications are given in Table 1. The Chandra source lists were filtered as follows. If the central X-ray source associated with the galactic nucleus was present, it was excluded from the list. Identified foreground and background sources as well as sources having statistically significant spatial extent were also excluded. With two exceptions we adopted the distances from the original X-ray publications. For NGC4697 we corrected the distance to 10.5 Mpc, the value determined recently by Mendez et al. (2001) based on planetary nebulae study. This distance is consistent with surface brightness fluctuation analysis and is significantly smaller than usually assumed value of 24 Mpc. For NGC5846 we used the distance of 24 Mpc as determined by Jensen et al. (2003) from I-band surface brightness fluctuation analysis.

The source detection in the original Chandra publications was carried out in different energy bands, and the count rates were converted to the energy flux under different assumptions regarding the source spectrum. This does not affect the growth curve analysis presented in section 3 but

<sup>1</sup> We compare bulge and disk population of X-ray sources in spiral galaxies in section 6.6

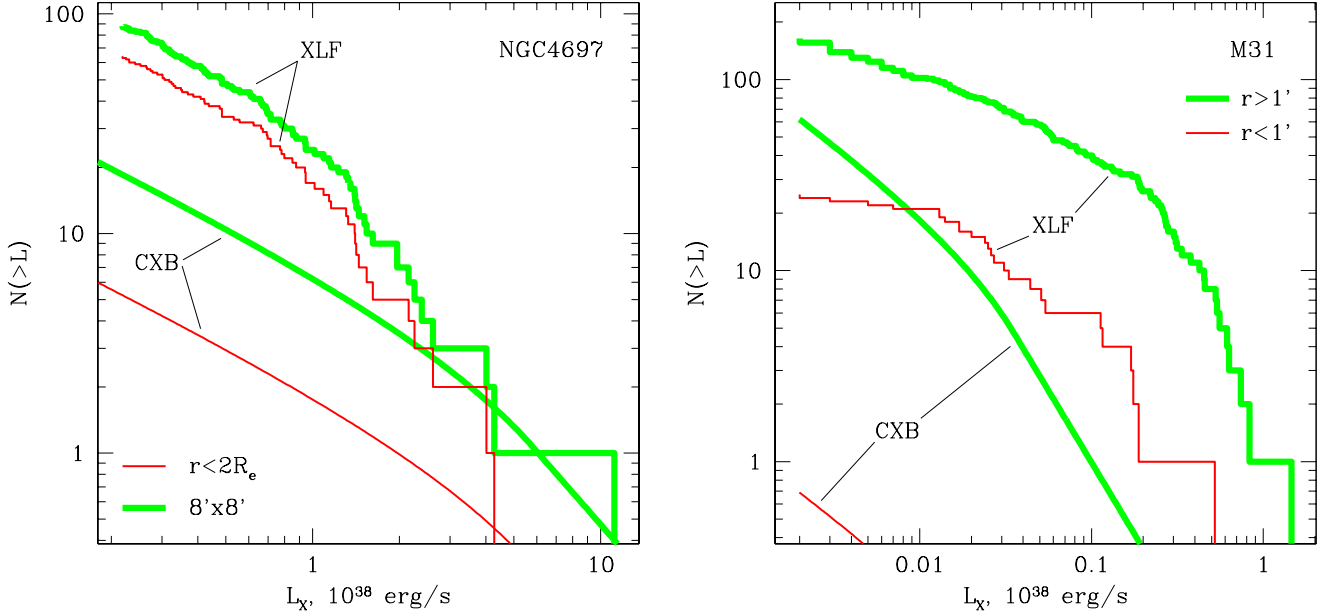


**Figure 1.** Illustration of importance of the contribution of CXB sources to observed XLFs of galaxies, depending on the shape of the luminosity function and the distance. *Left:* XLF of elliptical galaxy NGC4697 (distance 10.5 Mpc) obtained in a  $\sim 40$  ksec Chandra observation (Sarazin et al. 2001). The histograms show luminosity functions of the central 2 effective radii (thin histogram) and for entire ACIS-S3 chip ( $\sim 8' \times 8'$ , thick grey histogram), the solid lines show expected contribution of the background sources. Importance of the CXB contribution on the bright end of the luminosity function is apparent at large aperture. *Right:* Chandra ACIS-I observations of M31 (Kong et al. 2002) (distance 0.78 Mpc). The thin and thick lines and histograms correspond to central  $1'$  and it's exterior respectively.

might introduce additional systematic dispersion in studying the luminosity functions and X-ray-to-mass ratios. We estimate that in our sample of galaxies these uncertainties do not exceed  $\sim 20 - 30\%$  (cf. Maccarone et al. 2003). The difference in the source detection energy range could also introduce different spectra-dependent selection biases. However, considering the shape of the sensitivity curve of the Chandra ACIS detectors, and the energy ranges used for the source detection (with lower and upper boundaries in the range 0.3–0.5 and 7–10 keV) we do not expect significant systematic differences in the selection effects for the source samples obtained by different authors.

Important in constructing X-ray growth curves and luminosity functions is the completeness limit of the source lists. The point source sensitivity is affected by a number of factors. Most important in the context of studying the population of compact sources in galaxies are the degradation of the point spread function at large off-axis angles and the diffuse X-ray emission, the latter being especially significant for gas-rich elliptical galaxies. These effects might result in non-uniform sensitivity across the Chandra field of view and lead to apparent flattening of the luminosity function at the low luminosity end and distortion of the radial profile/growth curve (Fig.7, see also Finoguenov & Jones 2002; Kim & Fabbiano 2003). Whenever completeness analysis was performed in the original publication, the derived value of the completeness limit was used. In all other cases we assumed the completeness limit of  $\approx 2 - 3$  times of the detection sensitivity.

## 2.2 Contribution of CXB sources

In the central regions of the galaxies, the surface density of the compact sources is sufficiently high that the contribution of CXB sources (background AGNs) can be safely neglected. In outer parts, however, the surface density of X-ray binaries becomes comparable to or smaller than the average density of CXB sources (Fig.6) and the contribution of the latter needs to be taken into account. This plays an important role in studying the growth curves and X-ray luminosity functions within large aperture (c.f. Blanton et al. 2001; Finoguenov & Jones 2002; Kim & Fabbiano 2003).

To estimate the contribution of the CXB sources, we used results of the Chandra 1 Msec survey of the Chandra Deep Field South (Rosati et al. 2002). As the energy range for source detection included  $\sim 0.5 - 2$  keV energy range where the Chandra sensitivity peaks, we used the soft band counts, rescaling the flux to the energy band of the source list under consideration. Based on the results of the Chandra CDF-S survey the  $\log(N)$ – $\log(S)$  distribution of the CXB sources in the 0.5–2 keV energy range was assumed to have the form:

$$\frac{dN}{dS} = \begin{cases} KS^{-\alpha_1} & S < S_b \\ KS_b^{\alpha_2 - \alpha_1} S^{-\alpha_2} & S \geq S_b \end{cases} \quad (1)$$

where the break flux is  $S_b = 1.4 \cdot 10^{-14}$  erg/s/cm<sup>2</sup>, the differential slope before the break is  $\alpha_1 = 1.63 \pm 0.13$  and equals to Euclidean value after the break,  $\alpha_2 = 2.5$ . The normalization  $K = 291 \pm 20$  corresponds to  $N(S > 2 \cdot 10^{-15}) = 380 \pm 80$  sources/deg<sup>2</sup>. Note, that both  $S$  and  $S_b$  in eq.(1) refer to the 0.5–2 keV flux and are expressed in units of  $2 \cdot 10^{-15}$

erg/s/cm<sup>2</sup>. In order to use the above log(N)–log(S) relation to estimate the number of CXB sources  $N_{CXB}(S > S_{E_1-E_2})$ , the threshold flux  $S_{E_1-E_2}$  should be transformed to the 0.5–2 keV energy band and corrected for difference in the assumed spectral shape.

The importance of the CXB source contribution, especially when working with large aperture, significantly exceeding the effective radius of the galaxy, is illustrated in Fig.1. Due to the presence of a break in the log(N)–log(S) for background sources (corresponding to a luminosity of  $1.7 \cdot 10^{38} (d/10 \text{ Mpc})^2 \text{ erg/s}$ ) at which the slope changes by  $\Delta\alpha \sim 0.9 - 1$ , the contribution of the CXB sources depends critically on the galaxy distance. For relatively distant galaxies,  $D \gtrsim 10 - 15 \text{ Mpc}$ , it is more prominent at the high luminosity end of the XLF. Although existence of the ultra-luminous X-ray sources with luminosities exceeding  $\sim 10^{38} - 10^{39} \text{ erg/s}$  is beyond any doubts, Fig.1 (left panel) demonstrates that some fraction of them might be in fact background AGNs.<sup>2</sup> For nearby galaxies on the other hand, the contribution of CXB sources is more significant in the lower luminosity end of the XLF (Fig.1, right panel). This can, in particular, distort the slope of the XLF at low  $L_X$  in the outer parts of the galaxies.

An important factor that precludes the precise subtraction of the CXB contribution is clustering of the background sources on various angular scales, including sub-arcmin scales (e.g. Vikhlinin & Forman 1995) leading to significant field-to-field variations in their log(N)–log(S) distribution (e.g. Rosati et al. 2002; Manners et al. 2003). Another factor that complicates accounting for CXB contribution to the total luminosity is the effects of small numbers statistics (Grimm et al. 2003; Gilfanov et al. 2003), discussed in more detail in subsection 2.5.

### 2.3 Stellar mass

It is well-known, that the mass-to-light ratio in the near-infrared band is significantly less subject to the stellar population dependent variations than at the optical wavelength. Moreover, near-infrared light is much less affected by extinction:  $A_B/A_K \sim 10$ , where  $A_K$  and  $A_B$  are the extinction in the K- and B-band respectively (e.g. Fitzpatrick 1999). These make the near-infrared light a more robust estimator of the stellar mass than emission at shorter wavelengths.

Although to a lesser degree than optical, the near-infrared mass-to-light ratio bears some sensitivity (probably up to a factor of  $\sim 2$ , Bell & de Jong (2001)) on the properties of the stellar population i.e. on the star formation history of the galaxy. To compensate for this effect, we use the fact that variations of the mass-to-light ratio correlate tightly with the optical color of the galaxy (e.g. Brinchmann & Ellis 2000; Bell & de Jong 2001; Kauffmann et al. 2003). Specifically, the results of galaxy evolution modeling by Bell & de Jong (2001) relate the K-band mass-to-light ratio  $M_*/L_K$  to the  $B - V$  optical color:

$$\log(M_*/L_K) = -0.692 + 0.652(B - V) \quad (2)$$

<sup>2</sup> Note that the brightest ULX sources observed in the star-forming galaxies with  $\log(L_X) \gtrsim 39.5 - 40$  are less subject to CXB contamination than “dimmer” ULXs in ellipticals, having typically  $\log(L_X) \sim 38.5 - 39.5$ .

Although Bell & de Jong (2001) modeled disk systems in spiral galaxies, the slope of the  $M_*/L$ -color correlation is remarkably robust with respect to the uncertainties in the stellar population and details of the galaxy evolution, provided there is no systematic variation of the initial mass function with galactic type. Although the details of the IMF do not change the slope of the  $M_*/L$ -color relation, they significantly affect the zero point in eq.(2). A second factor affecting the  $M_*/L$ -color relation is strong recent bursts of star formation. This, however, is irrelevant in the context of old stellar systems in the nearby galaxies studied in the present paper. To conclude, the simple color based correction described by eq.(2) should, to the first approximation, account for the main trend in the stellar population dependent variations of the  $M_*/L$  ratio.

The extinction corrected B–V colors for the galaxies from our sample, adopted from the RC3 catalog (de Vaucouleurs et al. 1991) and corresponding K-band mass-to-light ratios computed using eq.(2) are listed in Table 1.

### 2.4 NIR multi-aperture photometry

The near-infrared multi-aperture photometry data were taken from the “Catalog of Infrared Observations, Edition 5” (Gezari, Pitts & Schmitz 1999). For all galaxies except two we used K-band measurements. In the case of M31 and M81, the data were insufficient for constructing meaningful growth curves in the K-band. Therefore we used H-band data and transformed it to K-band, using average NIR colors for normal galaxies  $\overline{H - K} = 0.2$  (Fioc & Rocca-Volmerange 1999). For several galaxies (NGC1316, NGC4472, NGC4697, M84/NGC4374, Cen A/NGC5128 and NGC5846) we complemented the Gezari et al. (1999) by the data from Pahre (1999). Absolute K-band magnitude of the Sun was assumed to be equal to  $M_{K,\odot} = 3.39$ . Multi-aperture photometry was used to construct the near-infrared growth curves, as described in section 3.2.

### 2.5 Statistics of small numbers – collective luminosity of a population of discrete sources

In many astrophysically relevant situations, a problem arises to count or measure the collective luminosity of an ensemble of discrete sources with a power law (or similar) luminosity function. Rigorous mathematical treatment of this problem, including the formulae convenient for practical applications, is given in Gilfanov et al. (2003). Below we present a brief qualitative consideration in the context of this paper.

Let us consider a population of compact sources (X-ray binaries in a galaxy or CXB sources projecting inside a galaxy) whose luminosity or flux distribution is a power law with differential slope  $\alpha$  and cut-off at  $L_{\text{cut}}$ :

$$\frac{dN}{dL} = \begin{cases} KL^{-\alpha} & L < L_{\text{cut}} \\ 0 & L \geq L_{\text{cut}} \end{cases} \quad (3)$$

The normalization of this distribution  $K$  might depend on such quantities as the mass of the galaxy (in the case of X-ray binaries) or the sky area (in the case of the CXB sources).

The quantity of interest is the total luminosity of all

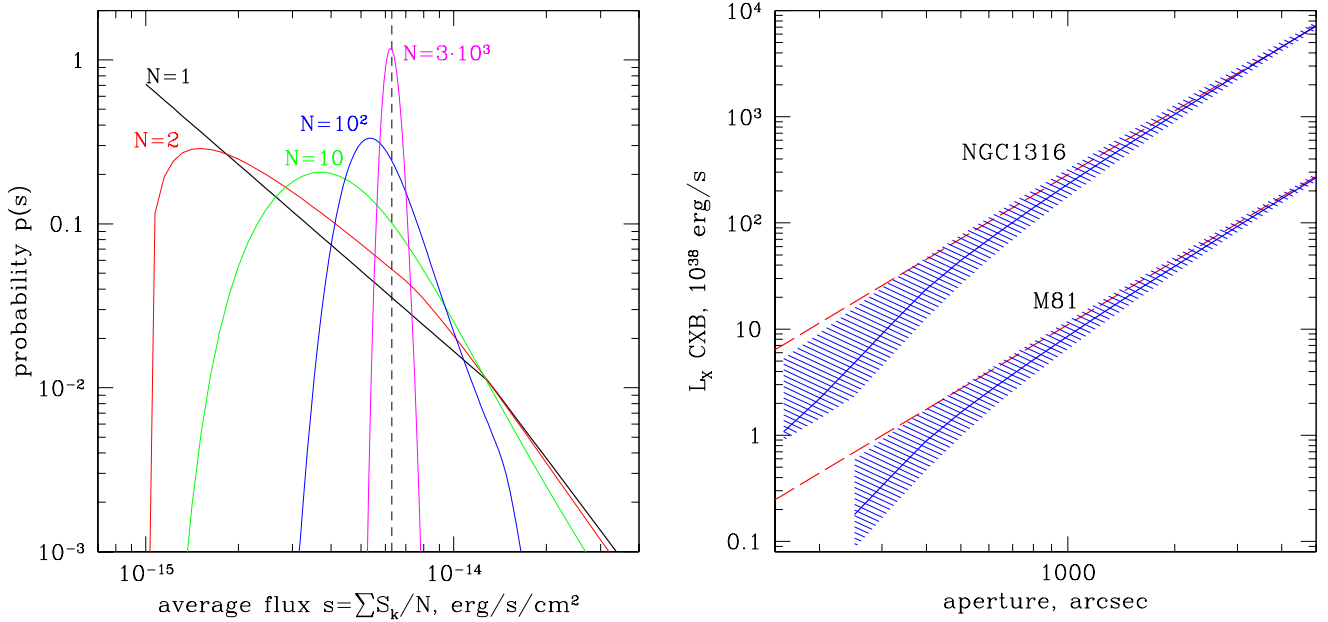


**Figure 2.** Illustration of the effects of small number statistics, using the integrated flux of the CXB sources as an example. *Left:* Probability distributions of average CXB source flux for various numbers of detected sources  $N$ . The assumed detection threshold was  $10^{-15}$  erg/s/cm<sup>2</sup> and the probability distribution of the flux of one source is the CXB log( $N$ )–log( $S$ ) as given by eq.(1). The vertical dashed line is the expectation mean (cf.eq.(5)). *Right:* Combined apparent luminosity of the CXB sources detected above the sensitivity limit  $L_{\min}$  as a function of aperture for NGC1316 ( $D=18.6$  Mpc,  $L_{\min} = 10^{38}$  erg/s) and M81 ( $D=3.6$  Mpc,  $L_{\min} = 10^{37}$  erg/s). The luminosity was computed assuming that CXB sources belong to the galaxy under consideration (i.e. are located at the same distance). The dashed straight lines show expectation mean, eq.(5) (cf. vertical dashed line in the left panel). The solid curved lines show the luminosity corresponding to the mode of the distribution, i.e. the most probable value of the integrated luminosity of the CXB sources. The shaded areas around the solid curves show 67% intrinsic uncertainty.

sources in the galaxy with luminosity exceeding a given detection limit  $L_{\min}$ :

$$L_{\text{tot}} = \sum_{L_k > L_{\min}} L_k \quad (4)$$

A seemingly obvious expression for the total luminosity can be obtained by integrating the luminosity distribution (3):

$$\langle L_{\text{tot}} \rangle = \int_{L_{\min}}^{L_{\text{cut}}} \frac{dN}{dL} L dL \propto K \quad (5)$$

This equation defines the expectation mean for  $L_{\text{tot}}$  and implies, that e.g. the total luminosity of the CXB sources is directly proportional to the sky area.

However, in the case of a “small” number of sources (the threshold value depending on the slope of the luminosity function and values of  $L_{\min}$  and  $L_{\text{cut}}$ ), the probability distribution  $p(L_{\text{tot}})$  might be strongly asymmetric, as illustrated by the left panel in Fig.2. Because of the skewness of  $p(L_{\text{tot}})$ , the most probable value of  $L_{\text{tot}}$  – the mode of the distribution, is not equal to the expectation mean defined by eq.(5). Importantly, it is the mode of the distribution  $p(L_{\text{tot}})$ , that would be most likely measured in an arbitrarily chosen galaxy.<sup>3</sup>

The difference between these two quantities is further

illustrated in the right panel in Fig.2 which shows the expected total luminosity of the CXB sources detected above the sensitivity threshold in the Chandra observations of NGC1316 and M81, as a function of aperture. As evident from Fig.2, the value of the total flux/luminosity of the CXB sources which will be most likely detected in these observations inside, for example, the effective diameter of the galaxy,  $\sim 100'' - 200''$ , deviates significantly from the expectation value given by eq.(5). It is correctly predicted by eq.(5) only for sufficiently large aperture (sky area), i.e. when sufficient number of sources are detected above the sensitivity threshold.

The mode of the probability distribution (the solid line in the right panel of Fig.2) is the value of the total luminosity which will most likely be measured in an arbitrarily chosen galaxy. If a number of observations of many (different) galaxies are performed, the obtained values of  $L_{\text{tot}}$  will obey the probability distribution depicted in the left panel of Fig.2. Consequently, strong and asymmetric dispersion among the measured values of  $L_{\text{tot}}$  should be expected, due to strongly asymmetric shape of the probability distribution. On rare occasions, for some of the galaxies, large values of the total luminosity would be observed, corresponding to the tail of the  $p(L_{\text{tot}})$ . The average of the measured values of  $L_{\text{tot}}$  will be equal to the expectation mean given by eq.(5).

<sup>3</sup> Obviously in the case of e.g. a flat ( $dN/dL = \text{const}$ ) or Gaussian

flux distribution, the most probable value of  $L_{\text{tot}}$  always equals the expectation mean defined by eq.(5).

### 3 X-RAY AND NIR GROWTH CURVES

#### 3.1 X-ray growth curves

In order to study the spatial distribution of X-ray binaries, we utilize circular aperture growth curves. The growth curves were constructed from the filtered source lists with the appropriate completeness limits applied, as detailed in subsection 2.1. They describe the number of sources,  $N_X(< a)$ , located inside circular aperture (diameter)  $a$  and their total luminosity,  $L_X(< a)$ .

Two considerations were taken into account in the growth curves analysis. First, the detection sensitivity might exhibit significant non-uniformity across the galaxy image and typically worsens towards the center of the galaxy. If not properly corrected for, this effect can lead to distortions in the apparent surface density of X-ray sources, as discussed in subsection 2.1. Precise correction of the growth curves requires knowledge of the  $\log(N) - \log(S)$  distribution. Another possible way to minimize this effect is to increase the lower luminosity limit for the source selection,  $L_{\min}$ . This, however, results in a significant decrease in the number of sources available for study. Instead, we chose to exclude the very central parts of the galaxies,  $\sim$  few tens of arcsec, from the analysis. An additional advantage of this approach is that it alleviates, to some extent, the problem of confusion which might become relevant in the very centers of even relatively nearby galaxies (indeed, an angular resolution of  $1''$  at the distance of 17 Mpc is equivalent to  $\sim 30'$  at the distance of our Galactic Center).

Secondly, in the outer parts of the galaxies, the contribution of the CXB sources becomes important. Its accurate subtraction is complicated by field-to-field variations and, in the case of the X-ray luminosity growth curves, by the effects of small number statistics. We therefore excluded from the analysis outer parts of the galaxies, where the surface density of the CXB sources becomes comparable with the surface density of X-ray binaries.

#### 3.2 NIR growth curves

The near-infrared growth curves were constructed from the K- and H-band multi-aperture photometry data following the approach of Fioc & Rocca-Volmerange (1999). Using the fact that the near-infrared magnitudes correlate almost linearly (but with a slope different from 1) with optical B-band magnitudes, the NIR growth curve can be approximated by

$$m(a) = m_T + s_0 B(X, T_p) \quad (6)$$

$$X = \log(a/A_e)$$

where  $m(a)$  is the near-infrared magnitude inside the aperture (diameter)  $a$ ,  $m_T$  is the total NIR magnitude of the galaxy,  $B(X, T_p)$  is the B-band growth curve of the galaxy as a function of the dimensionless aperture  $X$  and the B-band photometric type  $T_p$ ,  $s_0$  is a parameter characterizing the slope of the NIR – B-band correlation, and  $A_e$  is the B-band effective (half-light) diameter of the galaxy. The shape function  $B(X, T_p)$  was defined by Prugniel & Heraudeau (1998) as photometric type-dependent extrapolation between the de Vaucouleurs and the exponential profiles (see also Appendix A in Fioc & Rocca-Volmerange 1999).

The B-band photometric types of the galaxies were

adopted from the HiperLeda catalog (Prugniel & Heraudeau 1998). The effective diameters  $A_e$  are from RC3 catalog (de Vaucouleurs et al. 1991) and are listed in Table 1. The two unknown parameters of the NIR growth curves – total magnitude  $m_T$  and slope  $s_0$  were determined from the weighted least-square fits to the NIR multi-aperture photometry. The weights were defined as the inverse square of the deviation of the given measurement from the best fit growth curve and were determined via an iterative procedure as described in Fioc & Rocca-Volmerange (1999).

The values of  $s_0$  and  $m_T$  obtained from the fits to NIR data are listed in the Table 1. For several galaxies independent determinations of the total NIR magnitude were available, and we compared our best fit values of  $m_T$  with those published elsewhere and generally found reasonable consistency, within  $\sim 0.1 - 0.4$  magnitude. This is well within the typical disagreement between different measurements and does not significantly compromise the following comparison of the X-ray and NIR growth curves since the NIR photometric measurements in most cases overlap considerably in the aperture with the X-ray data.

In the case of the Cen A galaxy, no  $A_e$  is given in the RC3 catalog. An attempt to use the value from HiperLeda catalog ( $A_e \approx 752''$ ) resulted in a bad fit to the near-infrared photometric data and the value of the total K-band magnitude lies significantly outside the range of other measurements  $m_T \sim 4.4 - 5.0$  (Pahre 1999). We therefore adjusted the value of  $A_e$  to achieve a good fit and a consistent value of the total magnitude. Listed in the Table 1 is the resulting value of  $A_e \approx 239''$ .

#### 3.3 Comparison of the growth curves

The X-ray and NIR growth curves are presented in Figs. 3 and 4. The solid symbols are the multi-aperture NIR photometry data, the smooth solid curve going through the points is the best fit NIR growth curve (subsection 3.2). Both are scaled by the X-ray/NIR ratios determined as described below. The X-ray growth curves were constructed for the number of sources  $N_X(< a)$ , Fig. 3, and their collective luminosity  $L_X(< a)$ , Fig. 4, inside aperture (diameter)  $a$ . The thin histograms show apparent (observed) X-ray growth curves plotted using unbinned data, so that each step of the histogram corresponds to one source. The thin solid line in the lower-right part of the figures presents the growth curve for the CXB sources estimated as described in subsection 2.2. The shaded areas around NIR and CXB growth curves correspond to the 67% statistical uncertainty calculated assuming Poisson distribution for the number of sources and results of subsection 2.5 for their total luminosity. The field-to-field variations of the CXB  $\log(N) - \log(S)$  were not taken into account in computing the uncertainties.

The growth curves were analyzed and the X-ray/NIR ratios were determined in the annulus with the boundaries  $a_{X,1} - a_{X,2}$  indicated by the dashed vertical lines in Figs. 3, 4. The inner boundary of the annulus  $a_{X,1}$  was chosen to avoid the incompleteness effects in the central parts of the galaxies as discussed in subsection 3.1. It was fixed at the value of  $30''$  for the majority of the galaxies. For three galaxies larger values of  $a_{X,1}$  were adopted. A strong diffuse source is observed in the case of NGC4472 (Maccarone et al. 2003) – we used inner diameter of  $50''$ . NGC5846 is one of the two

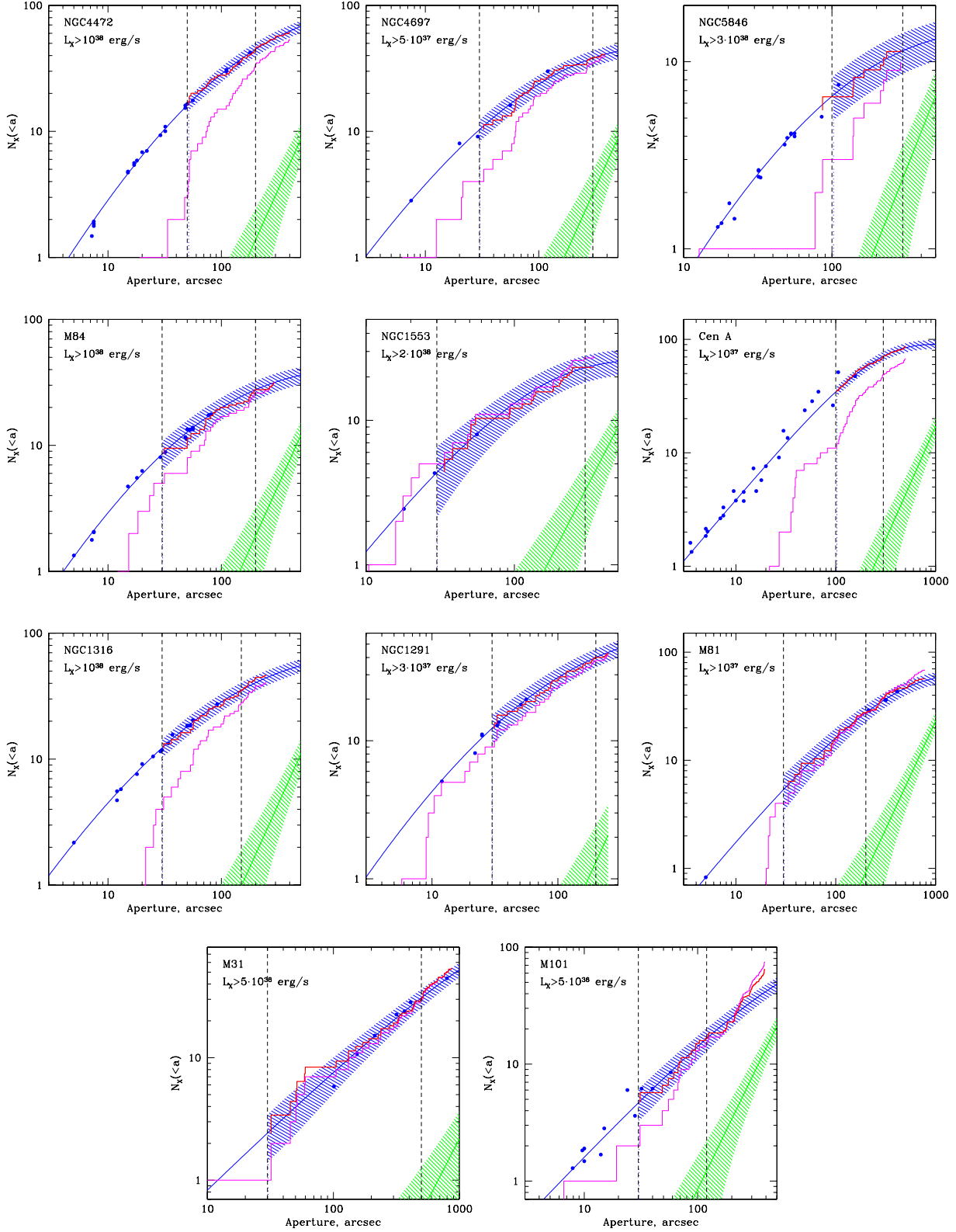


**Figure 3.** X-ray,  $N_X(< a)$ , (thick histogram) and near-infrared K-band (thin solid line) growth curves. The thin histograms show apparent growth curves for the number of sources with luminosity exceeding  $L_{X,min}$ , whose value is indicated in the upper-left corner of each plot. The thin solid line and shaded region in the lower-right corner of each panel show the CXB growth curve and its 67% statistical uncertainty. The solid circles are multi-aperture NIR photometry measurements, the thin solid curve and shaded area are the best fit NIR growth curve and its 67% statistical uncertainty. The NIR data and the growth curve were multiplied by  $N_X/L_{NIR}$  ratios determined in the annulus with boundaries  $a_{X,1}$  and  $a_{X,2}$  that are shown by the vertical dashed lines. The thick histogram shows the final corrected X-ray growth curve (see section 3.3 for details).

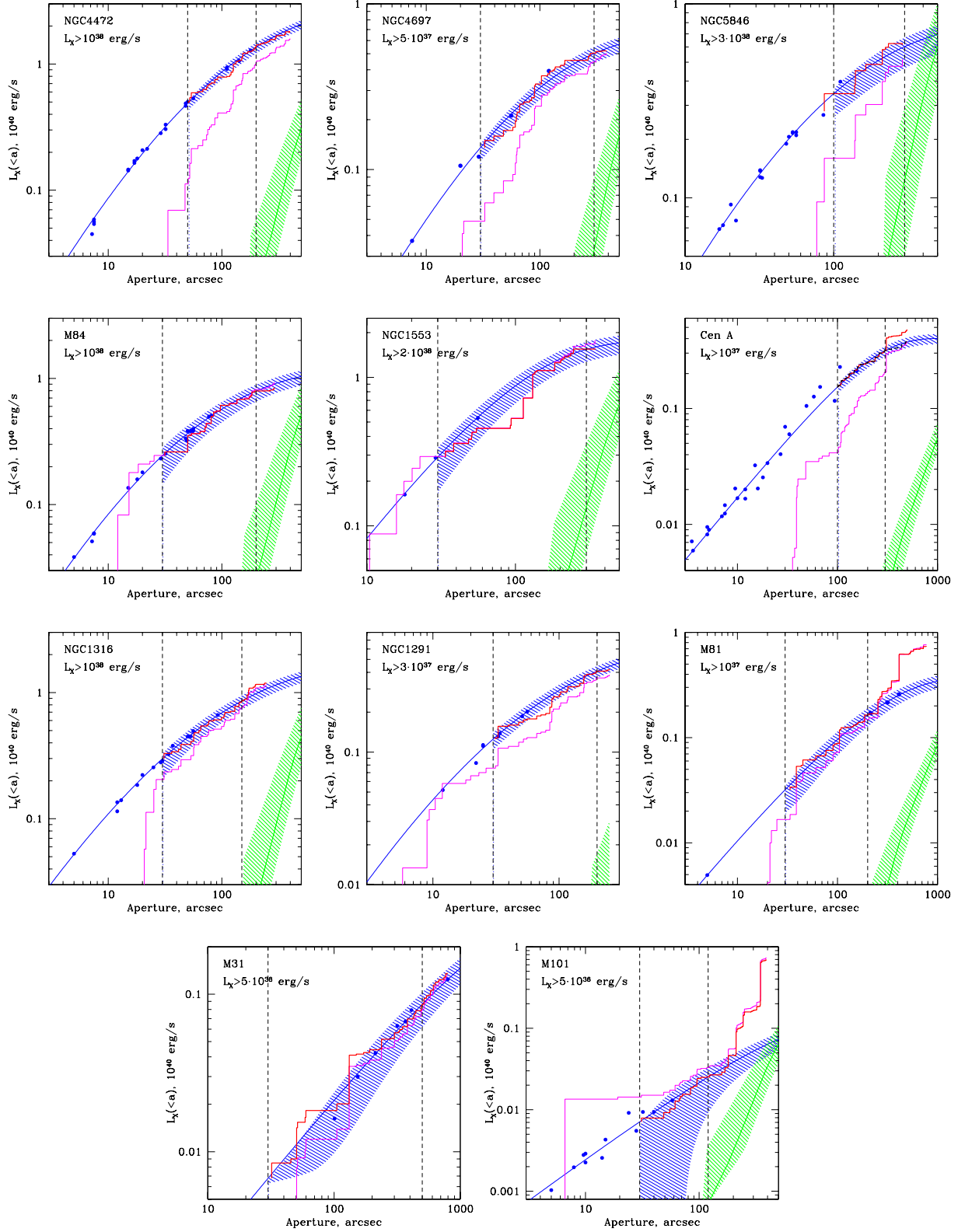


**Figure 4.** The same as Fig.3, but for the total X-ray luminosity  $L_X(<a)$ . See caption to Fig.3 for details.

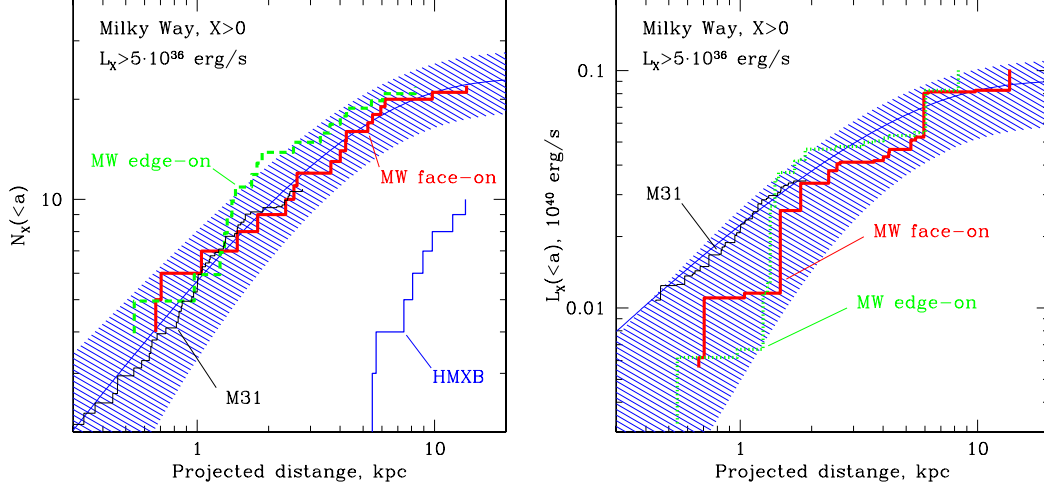


**Figure 5.** Growth curves for the number and total luminosity of LMXBs in the Milky Way compared with X-ray and near-infrared growth curves of M31. The growth curve of HMXBs in the Milky Way is also shown for comparison. Due to  $\sim 10$  times smaller number of HMXB sources in the Galaxy, a lower value of the threshold luminosity was chosen for them,  $L_X > 5 \cdot 10^{35}$  erg/s. In plotting the growth curves, only the sources in the half of the Galaxy, corresponding to  $X > 0$ , were selected (see section 3.5). The X-ray and NIR growth curves of M31 were normalized according to X-ray/NIR ratio of the Milky Way.

most distant and gas-rich (Trinchieri & Goudfrooij 2002) galaxies in our sample. Its X-ray growth curve shows an apparent decline inside  $\sim 100''$  (Fig.3). We attributed this decline to incompleteness effects and, in part, to confusion effects and assumed  $a_{X,1} = 100''$ . In the case of Cen A, the search for point X-ray sources in the inner part is complicated by the powerful jet emission. We therefore assumed  $a_{X,1} = 100''$ . The outer diameter  $a_{X,2}$  was constrained by either contribution of the CXB sources or by the boundaries of the CCD chip used in the analysis. It typically varied between  $\sim 150 - 300''$ . For the small bulge in the Scd galaxy M101 (Okamura et al. 1976), the outer boundary was chosen at  $a_{X,2} = 120''$  in order to minimize contribution of HMXBs (cf. Pence et al. 2001) in the derived X-ray/NIR ratios.

In calculating X-ray/NIR ratios, the number and luminosity of X-ray sources were corrected for the contribution of CXB sources. The near-infrared luminosity was computed integrating the best fit NIR growth curves. The boundaries  $a_{X,1} - a_{X,2}$  and derived X-ray and near-infrared parameters are listed in Table 2.

As evident from Fig.3 the growth curves for the number of X-ray sources agree well with the near-infrared ones. It is confirmed quantitatively by the results of the Kolmogorov–Smirnov test – the minimum values of K-S probabilities are 14% (NGC 1553) and 30% (M84) and are in the  $\sim 46 - 97\%$  range for other galaxies. To facilitate visual comparison of the growth curves, we plot as a thick histogram the X-ray growth curves shifted vertically to match the NIR curves at the inner boundary of the annulus  $a_{X,1}$ :

$$N_X(a) = N_X^{\text{obs}}(a) - N_X^{\text{obs}}(a_{X,1}) + N_X^{\text{pred}}(a_{X,1}) - (N_{X,\text{CXB}}(a) - N_{X,\text{CXB}}(a_{X,1})) \quad (7)$$

i.e. corrected for the expected number (luminosity) of the sources inside  $a_{X,1}$  and for the contribution of the CXB sources.

With few exceptions, the X-ray luminosity growth curves also agree well with the distribution of the near-infrared light (Fig.4). Significant deviations are observed in the case of Cen A and NGC1553, and, less prominent, in NGC1291. In the Cen A galaxy, the deviations are caused by a bright transient source with  $L_X \sim 10^{39}$  erg/s located at  $r \approx 150''$  from the nucleus, which changed its luminosity by a factor of  $\gtrsim 500$  between two Chandra observations separated by half a year (Kraft et al. 2001). If this source is excluded, the good agreement between X-ray and NIR growth curves is restored (dashed thick histogram in Fig.4).

In the case of NGC1553 and NGC1291, the X-ray growth curves appear somewhat “under-luminous” inside  $\sim$  effective radius of the galaxy. Interestingly, at larger radii the agreement with the NIR growth curves seems to be restored. The deviations are smaller in NGC1291,  $\sim 40\%$ , and are especially pronounced in NGC1553, reaching a factor of  $\sim 2$ . For the latter, we give in the Table 2 X-ray and NIR parameters for two different values of the outer radius  $a_{X,2}$ . The behavior of the  $N_X$  and  $L_X$  growth curves in these galaxies might indicate the presence of variations in the luminosity distribution of the sources with distance from the nucleus. As will be discussed in the following sections, luminosity distributions of compact sources in both galaxies appear to deviate somewhat from the average XLF (section 6.7).

### 3.4 Late type galaxies

The properties of X-ray sources in spiral galaxies appear to correlate with the properties of the surrounding stellar population (see Fabbiano & White 2003, for a review). The old stellar systems of bulges are dominated by low mass X-ray binaries, whereas the disk population might be significantly affected by ongoing star formation and, hence, a contribution of HMXB sources should be expected. These

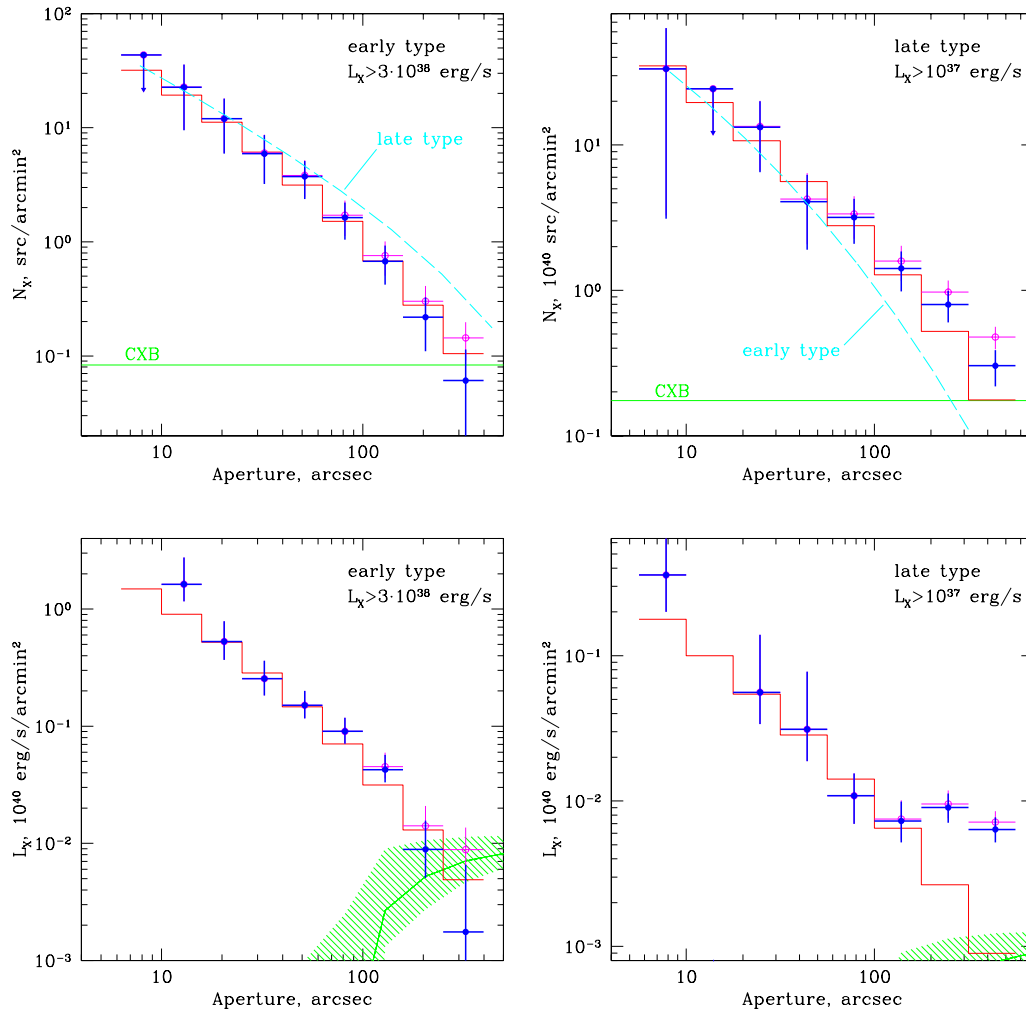


**Figure 6.** The differential radial profiles for the number of compact sources  $N_X$  and their collective luminosity  $L_X$ . *Left:* combined data for 4 early type galaxies (NGC4472, NGC4697, M84 and NGC1316). *Right:* combined profiles of two spiral galaxies (M81 and M101) with evidence of star formation outside the bulge. The thin open circles with error bars show observed profiles. The thick solid points with error bars show the profiles corrected for contribution of CXB sources. The latter is shown by thin solid line in the lower part of each panel, the shaded area in the lower graphs shows 67% statistical uncertainty. The histograms show radial profiles of the NIR light. For comparison, the radial profiles of late and early type galaxies are shown by dashed lines. The upper limits are 90% confidence.

expectations are supported by the spatial distribution of the compact X-ray sources in the disks of spiral galaxies, which often show a concentration towards the spiral arms (e.g. Pence et al. 2001; Grimm et al. 2002).

As the spatial distribution of HMXBs does not necessarily follow the stellar mass and, rather, correlates with the regions of star formation, the X-ray growth curves for spiral galaxies deviate significantly from the distribution of the near-infrared light outside the bulge (Fig.3 and 4). These deviations are mostly apparent for M81 and M101, having disk star formation at the level of  $\sim 1 M_\odot/\text{year}$ . The bulge size corresponds to the aperture of  $\sim 100'' - 150''$  for M101 (Okamura et al. 1976)) and  $\sim 450'' \times 240''$  ellipsoid in the case of M81 (Reichen et al. 1994). As the luminosity function of HMXBs has a cut-off at  $\sim 10$  times higher luminosity than LMXBs (section 4, Grimm et al. (2003)), the deviations are most apparent in the X-ray luminosity growth curves. The deviations are significantly less pronounced in the case of

M31 which has a larger angular bulge size,  $a \gtrsim 1000''$  (Morton et al. 2001; Fabbiano & White 2003), and smaller star formation rate within the Chandra field of view.

### 3.5 The Milky Way

Unlike external galaxies, the growth curves for the Milky Way cannot be directly constructed, because different sources are located at different distances. During the past decade, significant progress has been achieved in studying the bright X-ray binaries in the Galaxy. In particular, distances have been determined by various methods for a significant fraction of X-ray binaries brighter than  $\sim 10^{36}$  erg/s. This allowed Grimm et al. (2002) to reconstruct a 3-dimensional picture of the galactic X-ray sources. Progress in optical observations also has led to determination of the nature of the optical companion in the majority of these systems. As has been argued by Grimm et al. (2002), although

residual incompleteness effects are still in play, the sample of X-ray binaries with  $L_X > 10^{35.5-36}$  erg/sec located within  $\sim 10 - 12$  kpc from the Sun should be sufficiently complete.

In order to study the growth curve of the low mass X-ray binaries in the Milky Way, we use X-ray luminosities and the compilation of source distances from Grimm et al. (2002). The X-ray luminosities were determined by Grimm et al. (2002) from the 5 year average of the the RXTE/ASM light curves of individual sources. We selected the LMXBs in the half of the Galaxy corresponding to  $X > 0$ , where the origin of the Cartesian coordinate system coincides with the Galactic Center and the X-axis is directed towards the Sun (Grimm et al. 2002). As the similar problem of different distances to the different emitting regions arises in the near-infrared band as well, we used as a model for the Milky Way the NIR light distribution in M31 which is sufficiently similar to our Galaxy in size and morphological type. The resulting growth curves for face-on and edge-on views of the Milky Way are plotted and compared with the NIR and X-ray growth curves of M31 in Fig.5. Also shown for comparison is the growth curve for HMXB sources in the Milky Way. Good agreement in the Milky Way and M31 growth curves is apparent. On the other hand, it is obvious that the HMXB sources have a significantly different spatial distribution.

As the accuracy of the distance determination is unlikely to exceed  $\sim 10 - 20\%$  even in the best studied cases, we excluded the central 1 kpc from our calculation of the X-ray/ $M_*$  ratios. The X-ray and near-infrared parameters listed in Table 2 were calculated for a face-on view of the Galaxy using the LMXB sources located at  $X > 0$  and  $1 \text{ kpc} < R_{\text{proj}} < 10 \text{ kpc}$ , where  $R_{\text{proj}}$  is the projected distance from the Galactic Center for a face-on view. The edge-on projection gives somewhat higher values, by  $\sim 10\%$  for the number of sources and by  $\sim 30\%$  for their total luminosity. Note that the values of the near-infrared luminosity, stellar mass, number of low mass X-ray binaries and their total luminosity, given in Table 2, refer to the  $\lesssim$  half of the Galaxy.

### 3.6 Differential radial profiles

The total number of sources above the completeness limit in most of the galaxies is insufficient to construct meaningful differential radial profiles. Therefore, in order to study the differential distribution of X-ray binaries, we combined the data for several galaxies of similar morphological type. The resulting differential profiles for the number of sources and their total luminosity are shown in Fig.6 using combined data for 4 early type galaxies having sufficiently low completeness limit (NGC4472, NGC4697, M84 and NGC1316), and late type galaxies M81 and M101. The near-infrared profiles were computed accordingly, combining the individual NIR growth curves.

As was discussed in section 3.3, the growth curves, especially for the early type galaxies, appear to have a deficit of the sources in the central  $\sim 20'' - 40''$  (diameter), which was attributed to a combination of various factors affecting the completeness of the source samples. In order to check this assumption we compare the radial profiles for the combined data for early type galaxies constructed using different low luminosity limits  $L_{\text{min}}$  (Fig.7). As is evident from Fig.7, the radial profile for  $L_{\text{min}} = 10^{38}$  erg/s shows a clear deviation

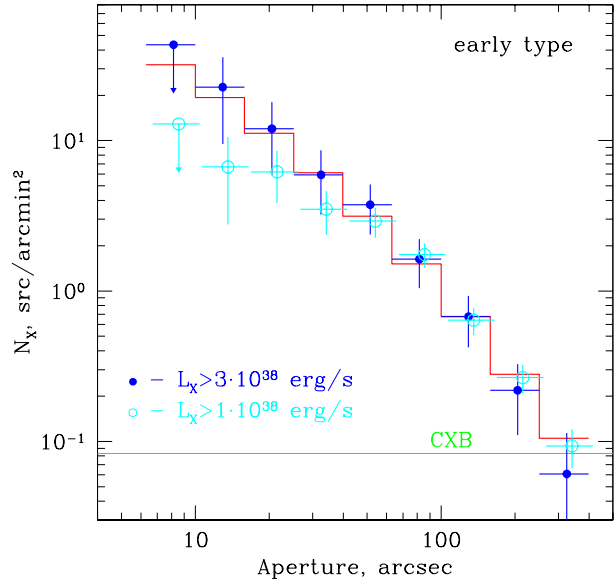


**Figure 7.** Illustration of incompleteness effects in the central part of elliptical galaxies. The points with error bars show differential radial profile of the number of sources for two different values of cut-off luminosity  $L_{X,\text{min}}$ . Contribution of CXB sources subtracted. The X-ray radial profile for  $L_{X,\text{min}} = 10^{38}$  erg/sec was rescaled according to the  $L_X/L_{\text{NIR}}$  ratio and shifted horizontally by a small offset for clarity. The histogram shows radial distribution of the NIR light. The horizontal line shows density of the CXB sources for cut-off luminosity  $L_{X,\text{min}} = 3 \cdot 10^{38}$  erg/sec.

from the NIR profile inside  $\sim 40''$ . Increasing  $L_{\text{min}}$  to  $3 \cdot 10^{38}$  erg/s leads to a radial profile consistent with the NIR profile. Although the luminosity dependent effects can not be presently excluded, it seems unlikely that such effects are responsible for distortion of the apparent radial profiles in the central part of galaxies. This conclusion is further supported by analysis of Finoguenov & Jones (2002) and Kim & Fabbiano (2003) showing that incompleteness effects due to the centrally concentrated diffuse emission can cause an apparent decrease of the number of detected sources in the central parts of the galaxies.

As might be expected from the growth curve analysis, there is good agreement between X-ray radial profiles and the distribution of the near-infrared light. For the spiral galaxies M81 and M101, deviation of the radial distribution from the NIR profile is evident outside the bulge, where star formation and HMXBs become important.

### 3.7 X-ray/NIR ratios

The X-ray/NIR ratios derived from the analysis of the growth curves have the advantage of being relatively free of a number of biases and incompleteness effects they could suffer otherwise. In particular they are not subject to incompleteness effects due to diffuse emission and source confusion in the central parts of the galaxies and are not affected by the contribution of CXB sources. The disadvantage, however is that they are obtained for different values of the luminosity threshold  $L_{\text{min}}$ . This is due to the fact that, for more dis-

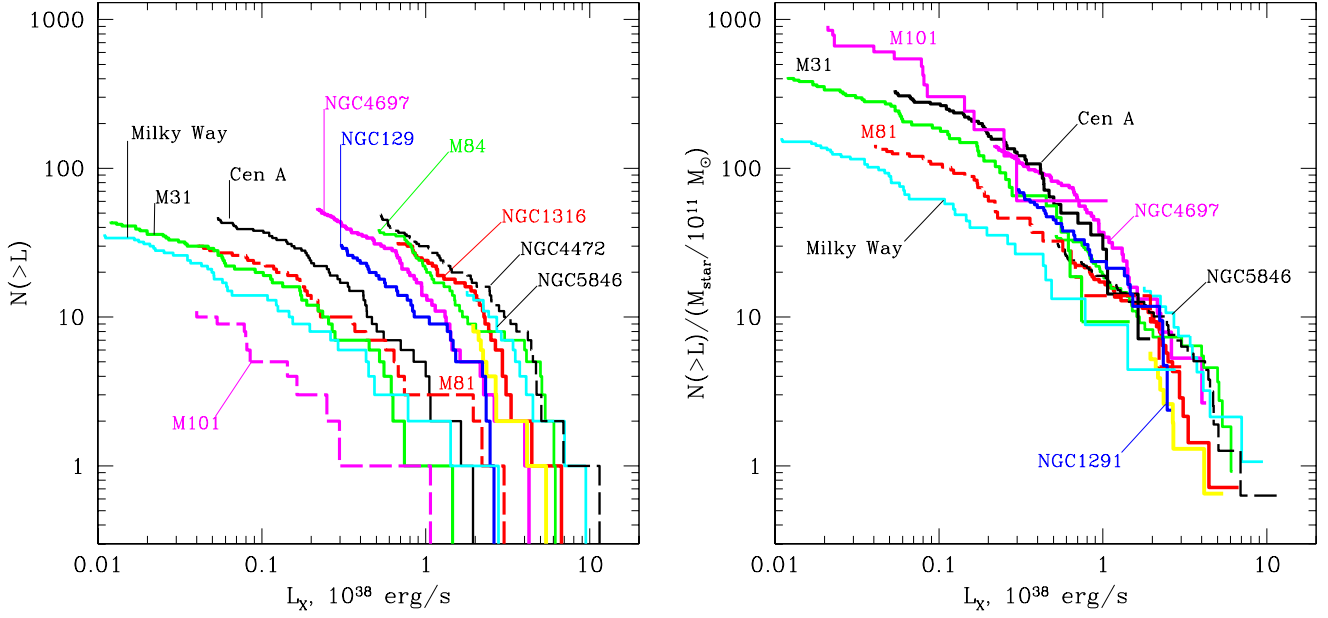


**Figure 8.** Cumulative X-ray luminosity functions for galaxies from our sample. *Left:* observed; *Right:* scaled by stellar mass. The luminosity functions were extracted in the annuli defined in the Table 2.

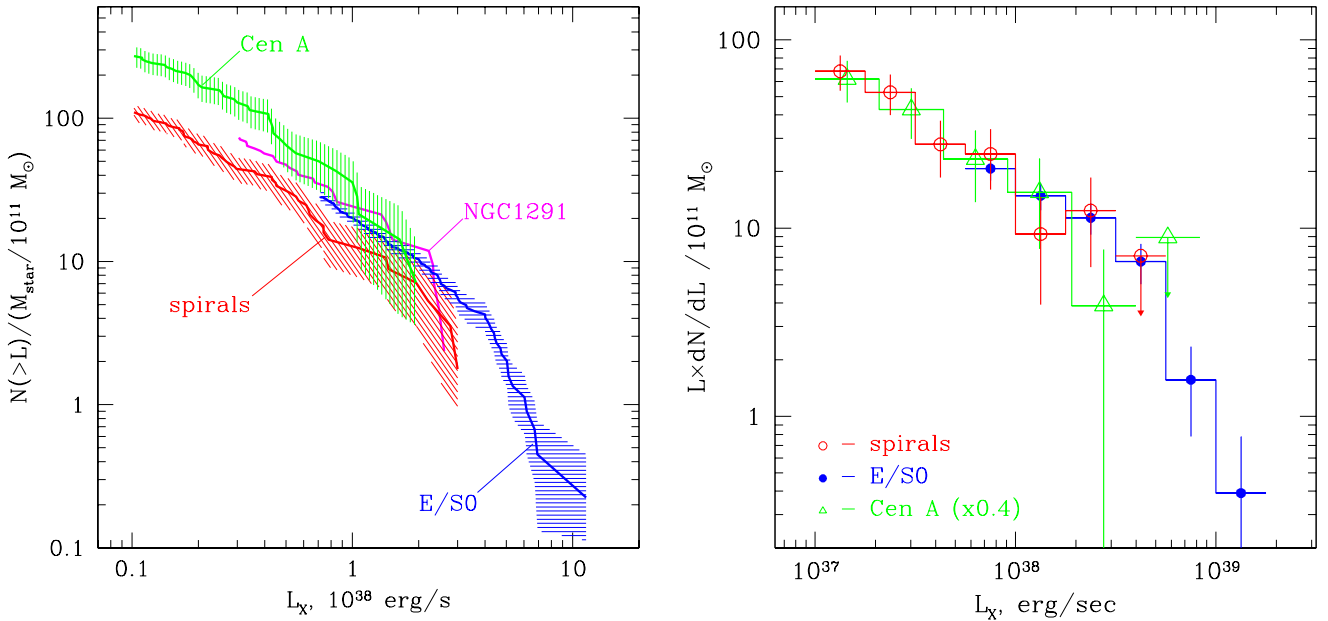


**Figure 9.** *Left:* Combined cumulative X-ray luminosity function for early type galaxies (NGC4472, NGC4697, M84 and NGC1316), spiral galaxies (M31, M81, M101 and the Milky Way) and Cen A galaxy, normalized to the stellar mass. The shaded areas indicate 67% uncertainty in the number of sources assuming Poisson distribution. *Right:* Differential luminosity functions for the same sets as in the left panel normalized to the stellar mass. To facilitate comparison of the shape, rather than normalization, the luminosity function of Cen A in the right panel is multiplied by a factor of 0.4. The upper limits in the right panel are 90% confidence.

tant early type galaxies, the Chandra sensitivity is typically  $\sim 10^{38}$  erg/s, whereas, in more nearby late type galaxies, the number of high luminosity sources is insufficient for meaningful analysis. For this reason the X-ray/NIR ratios cannot be directly compared for different galaxies from our sample and have to be corrected for difference in the threshold luminosity. This will be done in the section 5.

#### 4 X-RAY LUMINOSITY FUNCTION OF LMXBS

In order to study the X-ray luminosity functions, we use compact sources located in the annuli defined in section 3.3. The observed luminosity functions are shown in the left panel in Fig.8, with the luminosity functions normalized to the stellar mass in the right panel. As evident from Fig.8 the normalized XLFs occupy a rather narrow but still finite width band in the  $N(>L) - L$  plane. The difference in the number of sources is up to a factor of  $\gtrsim 3 - 4$  and is statistically significant. Note, that the Milky Way galaxy shows the largest deviation and is significantly below the main group. However, the shapes of the XLF for different galaxies are similar to each other, with the possible exception of NGC1553, which is discussed in detail in section 6.7. This is further illustrated by Fig.9 which shows the combined XLFs of early, late type galaxies and Cen A in cumulative and differential forms. Although the data for early and late type galaxies overlap in a rather narrow luminosity range near  $L_X \sim 10^{38}$  erg/s, it is obvious that they have close, although not identical, normalization. They also appear to have a similar slope below  $\sim \text{few} \times 10^{38}$  erg/s. This is further confirmed by the XLF of Cen A – the only early type galaxy whose luminosity function extends down to  $\sim 10^{37}$  erg/s.

Based on this evidence, we tentatively conclude that there is no significant difference in the shape of the XLFs above  $\sim 10^{37}$  erg/s between individual galaxies as well as in the combined data of early and late type galaxies.

##### 4.1 Low luminosity end of XLFs

Study of the X-ray luminosity function at low luminosities is complicated by the fact that for only two galaxies of late type – M31 and the Milky Way, does the data extend sufficiently below  $\sim 10^{37}$  erg/s. This range of luminosities is not covered at all in the observations of early type galaxies. Therefore any conclusion regarding the behavior of the XLF at low luminosities relies on a certain degree of extrapolation of the observational data.

We show in Fig.10 the XLFs of the galaxies from our sample in the differential form in a broad luminosity range from  $\sim 5 \cdot 10^{35}$  erg/s to  $\sim 10^{39}$  erg/s. As can be seen from the figure, there is significant flattening of the luminosity function below  $L_X \sim 10^{37}$  erg/s, observed in both M31 and the Milky Way. We emphasize that the luminosity functions for these two galaxies were constructed from entirely different datasets and therefore are subject to different systematic effects. The M31 luminosity function was obtained by Chandra (Kong et al. 2002) whereas the Milky Way luminosity function is based on the RXTE ASM data (Grimm et al.

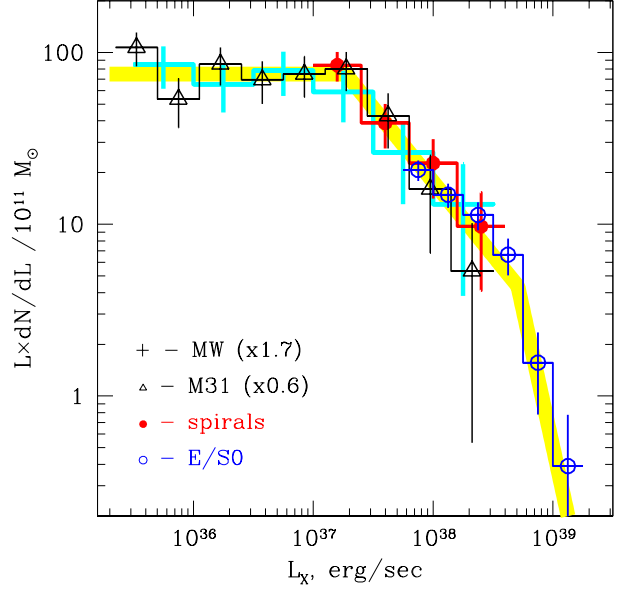


**Figure 10.** Differential luminosity function in a broad luminosity range. The combined data for early and late type galaxies (the same as in Fig.9) plotted along with XLFs of the central bulge of M31 and the Milky Way LMXBs. The XLFs of the Milky Way and M31 are multiplied by various factors (indicated in the parenthesis) to match each other in normalization. Note, that XLFs of the M31 and the Milky Way were obtained from Chandra and RXTE/ASM data respectively and are subject to different systematic effects. Since the XLF is plotted in units of  $LdN/dL$ , the flat part below  $\log(L_X) \sim 37$  corresponds to a differential slope of  $\sim 1$ . The thick grey line shows the template XLF defined in subsection 4.2.

2002). For both galaxies the completeness limit is substantially below  $\sim 10^{36}$  erg/s.

##### 4.2 Average XLF of LMXBs

In the following we assume that the luminosity functions of M31 and the Milky Way at the low luminosities are representative of the behavior common for all morphological types. As stressed in the previous subsection, this assumption involves a certain degree of extrapolation. NGC1553, showing somewhat peculiar behavior both in the  $L_X$  growth curves and in the X-ray luminosity distribution, is excluded from the analysis presented below in this subsection and will be discussed separately in the section 6.7.

The data plotted in Fig.10 indicate a rather complex shape of the combined luminosity function of LMXBs. To describe it quantitatively we define a template XLF as a power law with two breaks:

$$\frac{dN}{dL_{38}} = \begin{cases} K_1 (L_{38}/L_{b,1})^{-\alpha_1} & L_{38} < L_{b,1} \\ K_2 (L_{38}/L_{b,2})^{-\alpha_2} & L_{b,1} < L_{38} < L_{b,2} \\ K_3 (L_{38}/L_{cut})^{-\alpha_3} & L_{b,2} < L_{38} < L_{cut} \\ 0 & L_{38} > L_{cut} \end{cases} \quad (8)$$

where  $L_{38} = L_X/10^{38}$  erg/s and normalizations  $K_{1,2,3}$  are related by

$$K_2 = K_1 (L_{b,1}/L_{b,2})^{\alpha_2}$$

**Table 3.** Results of the maximum likelihood fits to the observed luminosity distributions by the template XLF, eq.(8)

sample	$L_{\min}$	$\alpha_1$	$L_{b,1}$	$\alpha_2$	$L_{b,2}$	$\alpha_3$
early type	$1 \cdot 10^{38}$	–	–	$1.64 \pm 0.22$	$5.1^{+1.4}_{-0.7}$	$5.0^{+2.3}_{-1.1}$
early type	$2 \cdot 10^{38}$	–	–	$1.80^{+0.61}_{-0.53}$	$5.1^{+1.9}_{-0.7}$	$5.0^{+2.8}_{-1.1}$
Cen A	$1 \cdot 10^{37}$	$1.0^f$	$0.2^f$	$1.96 \pm 0.23$	$5.0^f$	$5.0^f$
late type	$5 \cdot 10^{35} - 10^{37}$ (a)	$0.98 \pm 0.11$	$0.17^{+0.07}_{-0.03}$	$1.90^{+0.22}_{-0.15}$	$5.0^f$	$5.0^f$
all	$5 \cdot 10^{35} - 3 \cdot 10^{38}$ (b)	$1.0 \pm 0.13$	$0.19^{+0.06}_{-0.04}$	$1.86 \pm 0.12$	$5.0 \pm 0.7$	$4.8 \pm 1.1$

early type: NGC1316, NGC4472, NGC4697 and M84; late type: M81, M31, M101 and Milky Way;

all – all galaxies from Table 1, except NGC1553 (section 6.7);

$L_{\min}$  – minimum luminosity for ML fit;  $\alpha_1, \alpha_2, \alpha_3$  – differential slopes;  $L_{b,1}, L_{b,2}$  – first and second break in units of  $10^{38}$  erg/s (eq.8);

a –  $L_{\min}$ :  $5 \cdot 10^{35}$  erg/s (M31 and MW),  $5 \cdot 10^{36}$  erg/s (M101),  $1 \cdot 10^{37}$  erg/s (M81);

b –  $L_{\min}$ : the same as in (a) for late type galaxies, see Table 2 for other galaxies;

f – parameter was fixed at the quoted value.

$$K_3 = K_2 (L_{b,2}/L_{cut})^{\alpha_3}$$

The value of the high luminosity cut-off was fixed at  $L_{cut} = 500$ . Due to the steep slope of the luminosity function above  $L_{b,2}$ , the results are insensitive to the actual value of  $L_{cut}$ .

In order to determine the XLF parameters, we do Maximum Likelihood fits to the unbinned data for all galaxies from our sample, leaving the relative normalizations free. The best fit parameters are listed in the bottom line of Table 3 and the luminosity function is plotted as a thick grey line in Fig.10. The normalizations  $K_1$  for individual galaxies are shown as a function of the morphological type in Fig.11. The best fit value of the average normalization is:

$$K_1 = 440.4 \pm 25.9 \text{ per } 10^{11} \text{ M}_{\odot} \quad (9)$$

With this normalization, the cumulative number of sources computed integrating eq.(8)

$$N_X(> L) = \int_L^{L_{cut}} \frac{dN}{dL_{38}} dL_{38} \quad (10)$$

gives the number of sources per  $10^{11} \text{ M}_{\odot}$ . In cumulative form this normalization corresponds to the following values of the total number of sources with luminosity exceeding  $10^{37}$  erg/s and their collective luminosity:

$$N_X(> 10^{37} \text{ erg/s}) = 142.9 \pm 8.4 \text{ sources per } 10^{11} \text{ M}_{\odot} \quad (11)$$

$$L_X(> 10^{37} \text{ erg/s}) = (8.0 \pm 0.5) 10^{39} \text{ erg/s per } 10^{11} \text{ M}_{\odot}$$

To check for a possible dependence of the shape of the luminosity function on the morphological type, we also performed M-L fits to early and late type galaxies and Cen A separately. The best fit parameters are given in Table 3. As the late type galaxies data are insensitive to the XLF behavior above  $\gtrsim \text{few} \cdot 10^{38}$  erg/s, we fix the second break and slope at the values derived from all data combined together. Similarly, for the Cen A galaxy, we fix the first slope and break. As seen from Table 3, the early type galaxies show a somewhat flatter slope  $\alpha_2$  than late type galaxies or Cen A. The statistical significance of this difference is  $\sim 1\sigma$ . Increasing  $L_{\min}$  by a factor of two, from  $10^{38}$  erg/s to  $2 \cdot 10^{38}$  erg/s, reduces further this difference, indicating that it might be a result of residual incompleteness effects in the combined XLF of early type galaxies (c.f. Kim & Fabbiano 2003).

The results of the Kolmogorov-Smirnov test of the observed luminosity functions against the average XLF are

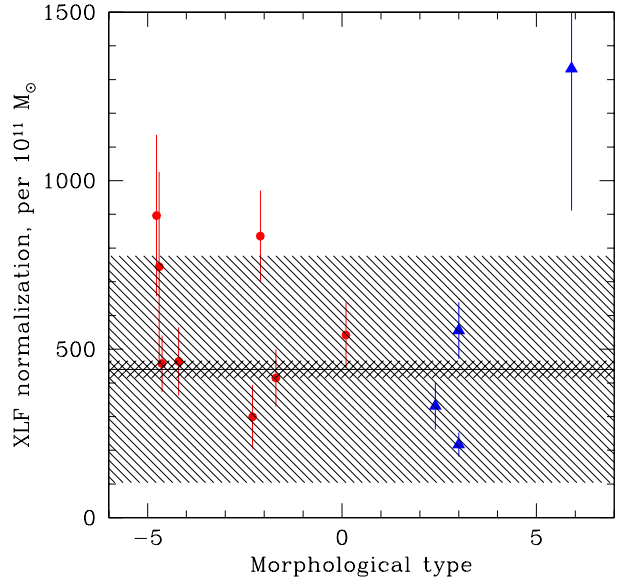


**Figure 11.** Normalization of XLF vs morphological type. Normalization is expressed in the same units as in eq.(9). The solid line and narrower shaded area show the average and its formal  $1\sigma$  error from eq.(9). The bigger shaded area shows the rms of the points with respect to the average. Note that this is essentially the same as the  $N_X/M_*$  plot shown in Fig.15. The only difference is that lower values of  $L_{\min}$  were adopted for MW, M31 and M101, whose points consequently have smaller error bars.

presented in Table 4. The good agreement between the observed and the average luminosity functions is further demonstrated in Fig.12, which can be regarded as an approximate graphical representation of the Kolmogorov-Smirnov test.

Finally, we construct the average LMXB luminosity function combining the data for all galaxies from our sample. We bin all the sources into logarithmically spaced bins and normalize the result by the sum of the stellar masses of all galaxies contributing to the given or previous luminosity bins. The advantage of this approach is that it allows us to combine the data with different completeness limits. The

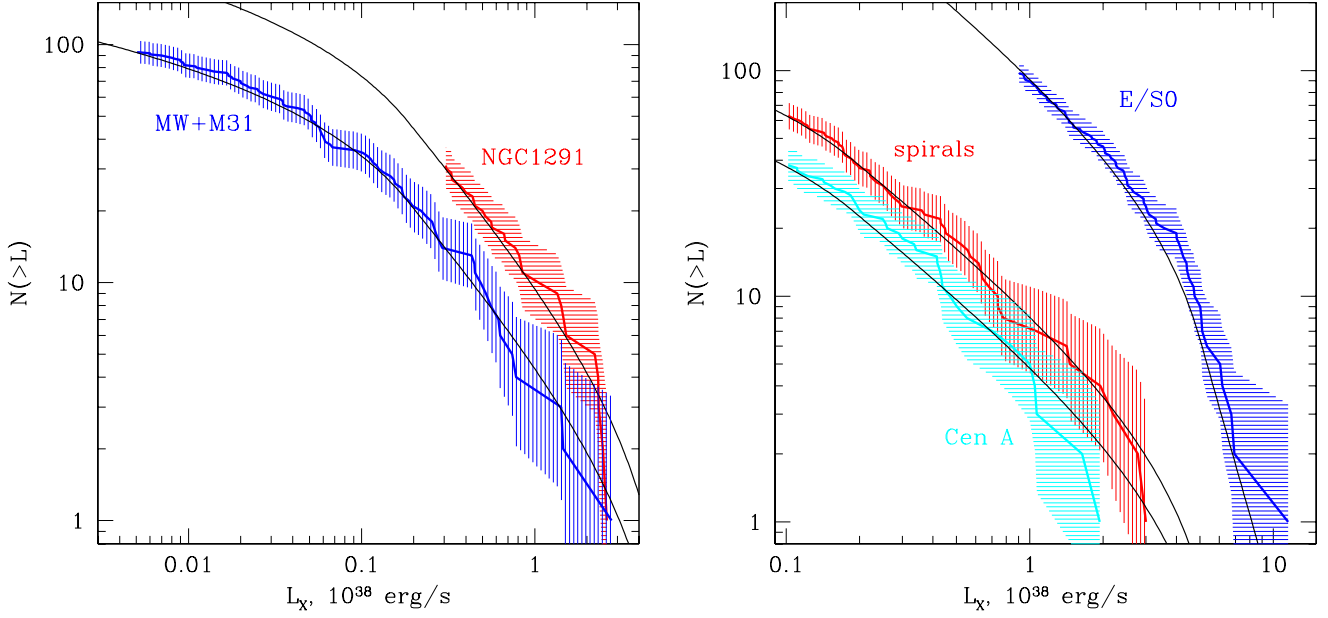


**Figure 12.** Comparison of the template XLF with the data. The shaded areas around the observed XLFs show the uncertainty of the Poisson distribution calculated using the prescription of Gehrels (1986). The solid lines show the template XLF with the parameters defined in subsection 4.2. To facilitate comparison of the shape, the normalization of the template XLF was adjusted to match the observed number of sources at the low luminosity end of each curve, irrespective to the stellar mass.

**Table 4.** The Kolmogorov-Smirnov test results for the template XLF

sample	$L_{\min}$	$N_{\text{src}}^a$	K-S prob. <sup>b</sup>
early type	$1 \cdot 10^{38}$	89	0.65
NGC 5846	$3 \cdot 10^{38}$	7	0.89
NGC1553	$2 \cdot 10^{38}$	22	0.16
Cen A	$1 \cdot 10^{37}$	38	0.92
NGC1291	$3 \cdot 10^{37}$	31	0.94
late type	$1 \cdot 10^{37}$	63	0.99
M31 + Milky Way	$5 \cdot 10^{35}$	95	0.74

The template XLF is defined by eq.(8) with the parameters from the bottom line of Table 3. early type: NGC1316, NGC4472, NGC4697 and M84; late type: M81, M31, M101 and Milky Way; a – number of sources; b – probability that observed XLF deviates from the model due to statistical fluctuations.

disadvantage, however, is that, due to significantly different luminosity ranges of the individual luminosity functions, uncertainties in the galaxy distance, stellar mass and intrinsic variations of the shape and normalization of the individual luminosity distributions may lead to the appearance of artificial features in the combined luminosity function. With that in mind, we plot the combined luminosity function in Fig.13.

In order to assess the amplitude of possible systematic uncertainties we performed Monte-Carlo simulations. In each run the distance of each galaxy and its mass-to-light ratio were replaced by random numbers drawn from a Gaussian distribution. The mean of the distribution was equal to the default value of the parameter and its  $1\sigma$  width was

set to 20% and 30% of the mean for the distance and the mass-to-light ratio respectively. If a negative number was drawn, it was rejected and the run repeated. For the Milky Way, the distance to each source was varied independently, assuming 20% relative uncertainty. For each bin of the luminosity function, the  $1\sigma$  systematic error was estimated as the rms of the values obtained in individual runs. The resulting 90% uncertainty regions are shown as the shaded areas in Fig.13.

## 5 X-RAY – STELLAR MASS RELATION

The average XLF of low mass X-ray binaries can be used to transform the X-ray luminosity and number of sources, computed with different completeness limits, to the same luminosity range. We chose the range  $L_X > 10^{37}$  erg/s in order to avoid the luminosity region where XLF shape is based on the late type galaxy data only. Such a choice helps avoid too large an extrapolation for early type galaxies, typically having higher completeness limits, and, on the other hand, allows a sufficient number of sources for late type galaxies, having smaller mass. The correction was done in the following way. Using the number of sources detected above the completeness limit for the given galaxy, we first determine the normalization of XLF. Then we use this normalization to calculate the expected number of sources and their total luminosity between the completeness limit and  $10^{37}$  erg/s. These quantities are listed in Table 2 and are added to the observed number of sources and to the sum of their luminosities.

For the derived shape of the average luminosity function, the luminosity correction does not exceed a factor  $\lesssim 2$

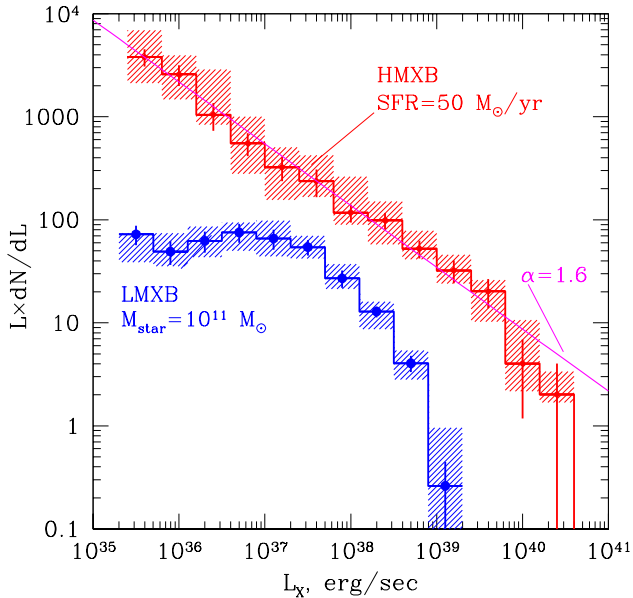


**Figure 13.** Average differential luminosity functions of high and low mass X-ray binaries. The HMXB XLF was adopted from Grimm et al. (2003) and scaled to the SFR=50  $M_{\odot}$ /year. The average LMXB XLF was constructed as described in section 4.2. The shaded areas around the luminosity functions illustrate the amplitude of systematic errors (90% confidence level) due to uncertainties in the source distance (assuming 20% relative uncertainty), mass-to-light ratios (30%) and star formation rates (30%).

for most of the galaxies, except for NGC5846, in which case it equals  $\approx 3.5$ . The correction factor is significantly larger for the total number of sources, generally up to a factor of  $\approx 15 - 20$  ( $\approx 40$  for NGC5846), making the estimates of the total number of sources significantly less robust. Note, that for the derived shape of the LMXB XLF, the luminosity of the sources above  $10^{37}$  erg/s accurately represents the total X-ray luminosity of the compact sources – the correction factor to the total luminosity is  $\approx 1.1$  (assuming that the luminosity function does not steepen at lower luminosities, below  $10^{35} - 10^{36}$  erg/s).

The number of sources with luminosity above  $10^{37}$  erg/s and their total luminosity is plotted as a function of the stellar mass in Fig.14. Early and late type galaxies are plotted by different symbols. To further illustrate that there is no significant difference between early and late galaxies we divide the early type galaxies into smaller annuli, whose mass is comparable to the typical masses of bulges in spiral galaxies. These are plotted in Fig.14 as open symbols.

We fit the  $N_X$ -mass and  $L_X$ -mass relations with a power law  $X = AM_*^\alpha$  using all galaxies from our sample (Table 2, solid symbols in Fig.14). We use  $\chi^2$  minimization, which is strictly applicable in the limit of a large number of sources per galaxy. This is correct for most of the galaxies from our sample (Table 2), therefore we do not expect any significant bias in the best-fit slope. The best fit values of the slope are consistent with unity:  $\alpha_{LX} = 1.01 \pm 0.06$  and  $\alpha_{NX} = 1.00 \pm 0.07$  for the luminosity and the number of sources respectively. We therefore

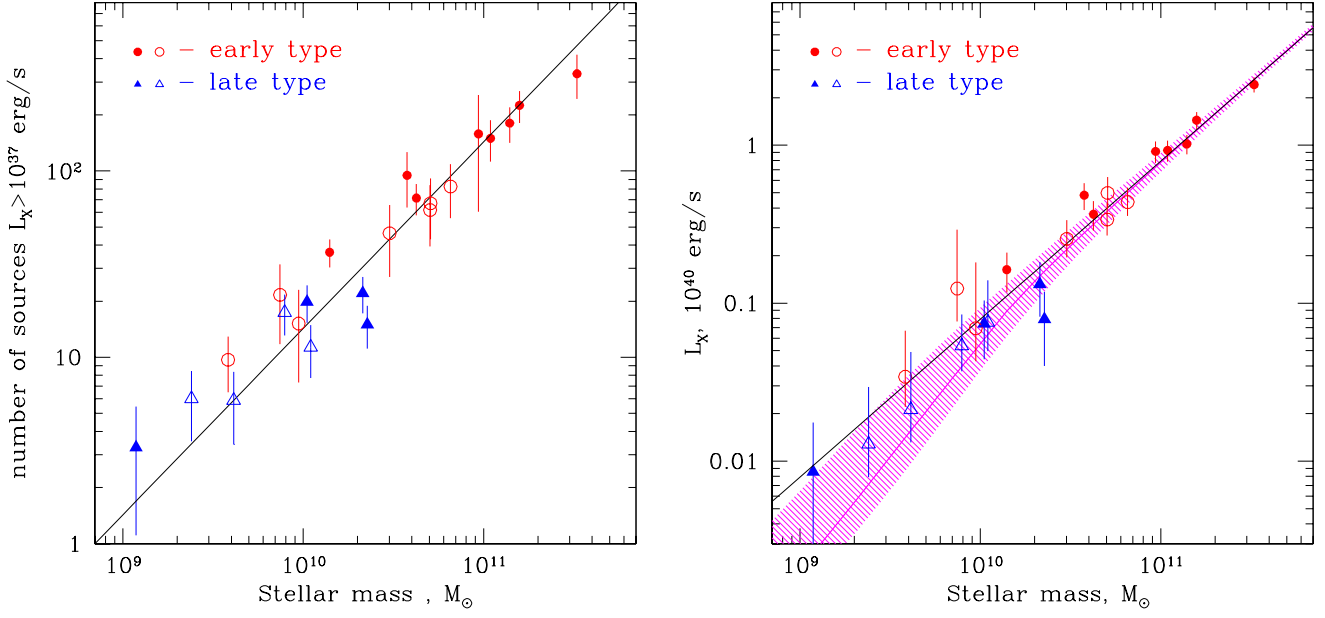
fix the slopes at  $\alpha = 1$  and consider average  $N_X/M_*$  and  $L_X/M_*$  ratios. To estimate these we use the unweighted average  $\langle X/M \rangle = \sum (X_i/M_i)/n$ . The results are given in Table 5 separately for early and late type galaxies and for all galaxies. Note that the average ratios given in Table 5 are not identical to those inferred from eq.(12), obtained integrating the average XLF, especially for  $N_X/M_*$  ratio. This discrepancy is due to difference between the expectation values of  $\langle X/M \rangle = \sum (X_i/M_i)/n$  and  $\langle X \rangle / \langle M \rangle = \sum X_i / \sum M_i$  in the presence of systematic errors. The systematic errors are present in both  $X_i$ , due to transformation to the same  $L_{min}$  based on the average XLF, and in  $M_i$ , as they are derived from near-infrared luminosity using an average color-based correction to mass-to-light ratio. The fact that we are dealing with rather small samples (e.g. 4 galaxies of late morphological type) also plays a role. For the same reason, yet different values would be obtained if one used weighted estimates for  $\langle X/M \rangle$ , e.g.  $\chi^2$  minimization technique. These factors should be taken into consideration when comparing the  $X/M_*$  ratios.

We show in Fig.15 the  $N_X/M_*$  and  $L_X/M_*$  ratios for individual galaxies as a function of the morphological type. As can be seen, there is statistically significant dispersion, of the order of  $\sim 25\%$  and  $\sim 40\%$  from the mean value for  $L_X/M_*$  and  $N_X/M_*$  respectively. A larger dispersion for  $N_X/M_*$  can probably be explained by the larger correction factors for the number of sources and, respectively, the stronger dependence of the correction factors on the details of the individual XLFs.

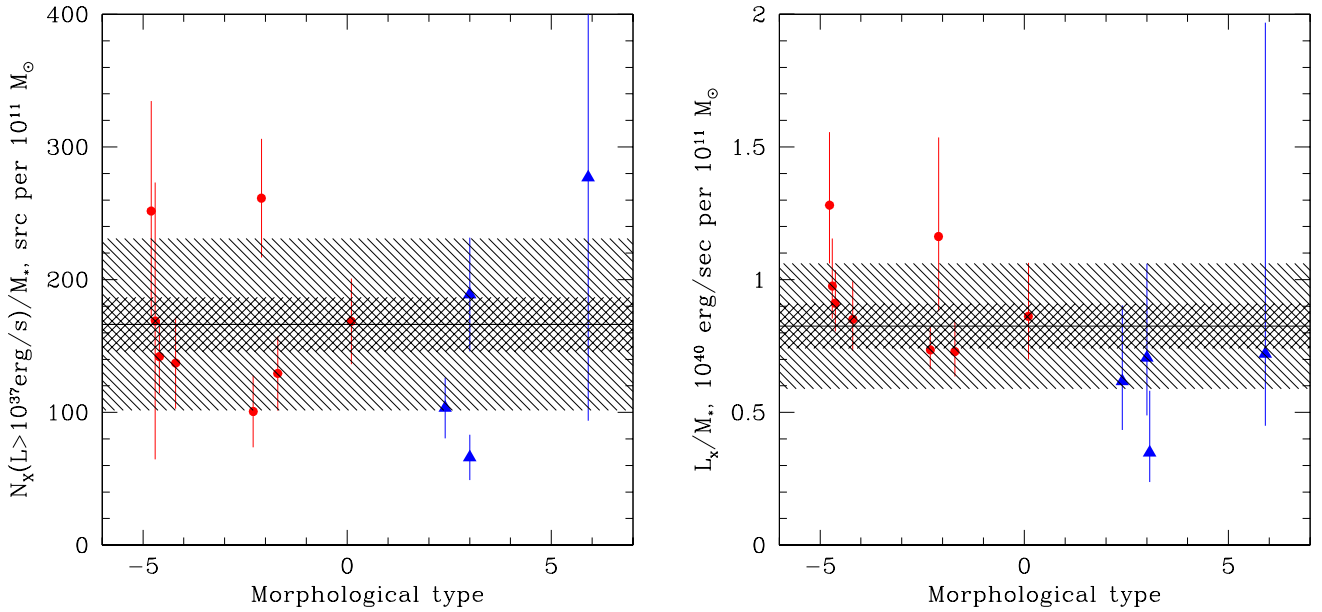
### 5.1 Dependence of the $X/M_*$ ratio on the morphological type ?

Fig.15 and Table 5 indicate a possible dependence of the  $L_X/M_*$  ratio on the morphological type. This can be in part caused by the statistical effects (section 2.5). Indeed, the bulges of spiral galaxies have smaller mass than early type galaxies, consequently, smaller numbers of luminous LMXB sources and, therefore, are more subject to the effects of statistics. That these effects can contribute to the observed trend is demonstrated by the last column in Table 5 where average  $L_X/M_*$  ratios, corrected for the statistical effects, are listed. An additional argument in favor of this explanation is that a similar trend is not observed for the  $N_X/M_*$  ratio (Fig.15, Table 5). On the other hand, the  $N_X/M_*$  ratios are more sensitive to the details of the individual luminosity functions and therefore are less robust.

Another factor might be insufficiently accurate calibration of the near-infrared mass-to-light ratios. As discussed in section 2.3, the color-based correction was obtained under the assumption of the universal initial mass function and might fail, if the morphological type dependent variations in the IMF are present (Bell & de Jong 2001). Such variations cannot be excluded a priori, given the broad range of morphological types in our sample. Yet another source of uncertainty is that in computing the  $M_*/L_K$  ratios integrated colors of the galaxies were used. As the galaxies do show color gradients (de Vaucouleurs & Corwin 1977; Prugniel & Heraudeau 1998), whose amplitude is type dependent and is largest for late types,  $2 \lesssim T \lesssim 5$ , this introduces additional uncertainty in the relative values of the  $M_*/L_K$  ratio derived for early and late type galaxies.



**Figure 14.** Number of sources with luminosity  $L_X > 10^{37}$  erg/s and their collective X-ray luminosity vs stellar mass. The data for galaxies from our sample (Table 2) are shown by solid circles and triangles for early and late type galaxies respectively. To further facilitate comparison of early and late type galaxies, several galaxies were divided into annuli of smaller size (i.e. containing smaller mass). These are shown by open symbols. Solid lines are linear relations given by eq.(12). On the right panel, the thick solid curve and the shaded area around it represent the relation between the stellar mass and the most probable value of the total luminosity and its 67% intrinsic uncertainty, obtained from the average XLF derived in subsection 4.2.



**Figure 15.**  $L_X/M_*$  and  $N_X/M_*$  ratios vs morphological type. The solid lines and narrower shaded areas show average and its formal  $1\sigma$  error from Table 5. The error was computed using statistical errors of the individual data points. The bigger shaded areas show rms of the points with respect to the average.  $L_X/M_*$  are not corrected for the effects of statistics.

**Table 5.** Average  $X/M_*$  and  $X/L_{\text{NIR}}$  ratios

sample	$N_X/L_{\text{NIR}}$	$L_X/L_{\text{NIR}}$ (a)	$N_X/M_*$	$L_X/M_*$ (a)	$L_X/M_*$ (b)
early type	$135.0 \pm 15.9$	$0.75 \pm 0.05$	$170.0 \pm 19.5$	$0.94 \pm 0.07$	$0.98 \pm 0.07$
late type	$81.2 \pm 19.6$	$0.33 \pm 0.10$	$158.8 \pm 47.6$	$0.60 \pm 0.21$	$1.04 \pm 0.22$
all	$117.0 \pm 12.4$	$0.61 \pm 0.05$	$166.3 \pm 20.5$	$0.83 \pm 0.08$	$1.00 \pm 0.08$

a – observed; b – corrected for the effects of statistics;

$N_X/M_*(L_{\text{NIR}})$  – in units of src per  $10^{11} M_\odot$  ( $L_\odot$ );  $L_X/M_*(L_{\text{NIR}})$  – in units of  $10^{40}$  erg/s per  $10^{11} M_\odot$  ( $L_\odot$ );

$N_X$  and  $L_X$  – number and total luminosity of X-ray sources brighter than  $10^{37}$  erg/s

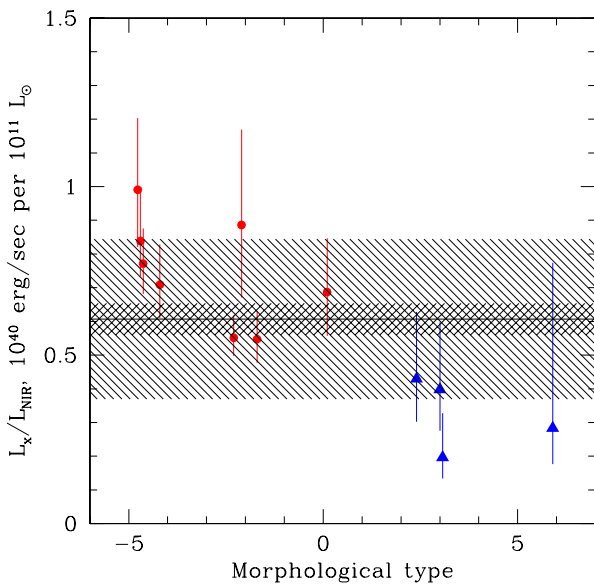


**Figure 16.**  $L_X/L_{\text{NIR}}$  ratios vs morphological type. The solid line and narrower shaded area show the average and its formal  $1\sigma$  error. The error was computed propagating the errors of the individual data points. The bigger shaded area shows the rms of the points with respect to the average. The  $L_X/L_{\text{NIR}}$  ratios are not corrected for the effects of statistics.

To conclude, due to a number of uncertain factors involved, the possibility of a weak dependence of the X-ray/mass ratios on the morphological type can be neither rejected nor confirmed with sufficient confidence. However, if present, it does not exceed a factor of  $\sim 1.5 - 2$ .

Interestingly, the X-ray/ $L_{\text{NIR}}$  ratios do show clear dependence on the morphological type (Fig.16). This is obviously caused by dependence of the near-infrared mass-to-light ratio on the morphological type of the galaxy. The correlation of the X-ray to optical light ratios with the morphological type should be significantly more pronounced at shorter wavelength, e.g. in the B-band, due to significantly stronger type dependent variations of the mass-to-light ratio in the optical band (Bell & de Jong 2001).

## 6 DISCUSSION

### 6.1 Is the average LMXB XLF universal?

Obviously, the shape of the luminosity function is defined by a number of factor which can vary from galaxy to galaxy. Of these effects, most important should be the effects of binary evolution. Despite of a number of population synthesis models developed, there is no a clear prediction about the evolution of the luminosity distribution of X-ray binaries with time. Based on simple arguments, one might expect that these effects are mostly pronounced at the high luminosity end of the XLF. Indeed, a luminosity of  $10^{38}$  erg/s requires a mass accretion rate of  $\sim 10^{-8} M_\odot/\text{yr}$ , which can be sustained by a low mass star for less than  $\lesssim 10^8$  yrs (Podsiadlowski et al. 2002). This value is significantly shorter than the life time of a galaxy. It is yet shorter for the most luminous LMXB systems with  $L_X \sim 10^{39}$  erg/s. In order to have the presently observed shape of the luminosity distribution, with a moderate fraction of sources with  $L_X \gtrsim 10^{37-38}$  erg/s, in the stellar systems of the age of  $\sim 10^{10}$  yrs, a continuous replenishment of the high luminosity sources is required.<sup>4</sup> Such replenishment can be maintained for example due to binary systems with initially less massive companion stars, reaching the X-ray active phase at later times. Clearly, evolution of the luminosity function with time must be present and it should be more pronounced at the high luminosity end of XLF. Consequently, no universal luminosity function in the strict sense should be expected, from which the source populations observed in different galaxies are drawn.

However, the results of the present study suggest that there are no significant variations of the shape of the luminosity distribution of low mass X-ray binaries in majority of nearby galaxies – they are broadly consistent with having the same shape. This fact might be somewhat surprising in the view of the arguments presented above. An obvious explanation is that the nearby galaxies constituting our sample have similar age of the stellar population, with sufficiently long time passed since the last starburst events. On the other hand, the departures from the average XLF possibly observed in NGC1553 and NGC1291 (section 6.7), if real, might be a manifestation of the XLF dependence on the age and star formation history of the host galaxy.

In interpreting the absence of pronounced systematic variations of the shape of the luminosity distribution, one

<sup>4</sup> Another possibility, considered by Piro & Bildsten (2002) is that the brightest LMXBs are transient sources with sufficiently low duty cycle,  $\sim 10^{-2} - 10^{-3}$ .

should take into consideration the sensitivity limitations of the present analysis. Indeed, in order to minimize contamination by the background sources and interference of the CCD boundaries, we analyzed the central parts of the galaxies, within  $\sim 1.5\text{--}2$  effective radii for the early type galaxies, and inner bulges for spirals. This resulted in a rather limited number of sources in our sample,  $\sim 350$  in total, and, consequently, to a limited sensitivity to possible XLF variations. The amplitude of the statistical uncertainties is illustrated by the shaded area in Fig.12. With increased sample and detection sensitivity, more complex behavior and more subtle effects can be discovered. We should note, however, that the analyzed annuli encompass from  $\sim 30\%$  to  $\sim 70\%$  of the total near-infrared luminosity (and stellar mass) of the galaxies. Typically, more than a half of the remaining stellar mass is contained in the central parts of the galaxies, inside the inner boundary of the analyzed annuli. On the other hand, for many galaxies the outer boundary was sufficiently close to the maximum value allowed by CXB contribution, especially for the luminosity growth curves. Therefore a significant increase of the number of X-ray binaries suitable for analysis would require an adequate improvement in the sensitivity and an accurate treatment of the incompleteness effects in the centers of the galaxies.

Due to typically larger distances to the elliptical galaxies, the low luminosity end of the XLF was studied using the data of only two late type galaxies, M31 and the Milky Way. Generalization of these results on the galaxies of all morphological types involves certain degree of extrapolation of the data. On the other hand, the old stellar systems in the ellipticals and spirals are similar in many respects and such an extrapolation might be justified.

## 6.2 X-ray luminosity function of low and high mass X-ray binaries

As was shown by Grimm et al. (2003), in a very broad range of luminosities,  $\log(L_X) \sim 35.5\text{--}40.5$ , the luminosity function of HMXBs is consistent, to the first approximation, with a single slope power law with the differential slope of  $\alpha_{\text{HMXB}} \approx 1.6$ . The average luminosity function of LMXBs, on the contrary, has a complex shape. It is a power law with the differential slope of  $\approx 1$  at low luminosities, steepens significantly at  $\log(L_X) \sim 37.5$  and has a cut-off at  $\log(L_X) \sim 39.0\text{--}39.5$  (Fig.13).

Different shape of the luminosity functions of the high and low mass binaries reflects, obviously, the difference in the accretion regimes. The majority of high mass systems are wind accretors. It has been shown by Postnov (2003), that the expected XLF slope is  $\sim 1.5$ , i.e. close to the observed value. Note, that Postnov's derivation was based on the assumption, that the mass distribution of the donor stars in HMXBs can be described by the Salpeter IMF. The low mass systems, on the other hand, are close binaries fed via Roche lobe overflow. The slope of the average LMXB XLF at  $\log(L_X) \gtrsim 37$  is qualitatively similar to that obtained by Pfahl et al. (2002) from X-ray binaries population synthesis,  $\alpha \sim 1.5\text{--}2$ . At lower luminosities, however, the population synthesis model predicts significantly more sources than actually observed. As discussed by Pfahl et al. (2002), the number of low luminosity sources is substantially reduced, if the irradiation of the donor star by the X-ray emission from

the primary is taken into account. Indeed, their illustrative  $\dot{M}$  distribution with simplified account of the irradiation effect is significantly flatter below  $\log(L_X) \sim 37$  and is qualitatively similar to the observed average XLF of LMXBs.

## 6.3 Diagnostics of on-going star formation

The different shape of XLFs of HMXBs and LMXBs can be used to diagnose on-going star formation in relatively nearby galaxies ( $\sim 20\text{--}30$  Mpc for the Chandra angular resolution). Two possibilities can be exploited.

The cut-off in the HMXB luminosity function occurs at  $\sim 10$  times higher luminosity than in LMXBs (Fig.13). In our sample of  $\sim 350$  sources in the old stellar systems with total stellar mass of  $\sim 10^{12} M_\odot$  two brightest sources, in NGC1553, have luminosity  $\sim 3.3 \cdot 10^{39}$  and  $\sim 2 \cdot 10^{39}$  erg/s (see sections 3.3 and 6.7.1). These two sources excluded, the luminosity of the other sources does not exceed  $\sim 10^{39}$  erg/s (Fig.8). The brightest high mass X-ray binaries, on the other hand, have luminosities up to  $\sim (2\text{--}3) \cdot 10^{40}$  erg/s. Detection of even one source with luminosity of the order of  $\sim 10^{40}$  erg/s or greater implies that the star formation process is taking place. From the number of such luminous sources the star formation rate can be estimated, as it is directly proportional to the SFR (Grimm et al. 2003):

$$N(L > 10^{40} \text{ erg/s}) \approx 1.2 \times \frac{\text{SFR}}{10 M_\odot/\text{yr}}$$

$$N(L > 5 \cdot 10^{39} \text{ erg/s}) \approx 2.9 \times \frac{\text{SFR}}{10 M_\odot/\text{yr}}$$

where SFR refers to the formation rate of stars more massive than  $\sim 5 M_\odot$ . This, obviously, can be used for sufficiently high star formation rates, exceeding  $\sim 10 M_\odot/\text{yr}$ .

Non-detection of luminous sources, on the other hand, immediately constrains the star formation rate, e.g. absence of sources with  $L_X > 5 \cdot 10^{39}$  or  $L_X > 10^{40}$  erg/s results in upper limit on the star formation rate of  $\text{SFR} \lesssim 8$  and  $\text{SFR} \lesssim 20 M_\odot/\text{yr}$  respectively (90% confidence level).

At lower star formation rates one can use the fact, that the XLF slopes at the low luminosity end are substantially different,  $\approx 1.0$  and  $\approx 1.6$  for LMXBs and HMXBs respectively (Fig.13). Therefore detection of a population of compact sources with sufficiently steep  $\log(N) - \log(S)$  distribution at  $L_X \lesssim 10^{37}$  erg/s might indicate on-going star formation. Conversely,  $dN/dS \propto L^{-1}$  distribution in the low luminosity limit would indicate that the X-ray emission is dominated by an old stellar population.

## 6.4 Relative contributions of high and low mass X-ray binaries

Relative contributions of low and high mass X-ray binaries to the observed population of compact X-ray sources is defined by the ratio of the stellar mass to the star formation rate. Due to different shapes of the luminosity functions (Fig.13) it also depends on the considered luminosities range.

Using the calibrations of  $L_X\text{--SFR}$  and  $L_X - M_*$  relations obtained by Grimm et al. (2003) and in the present

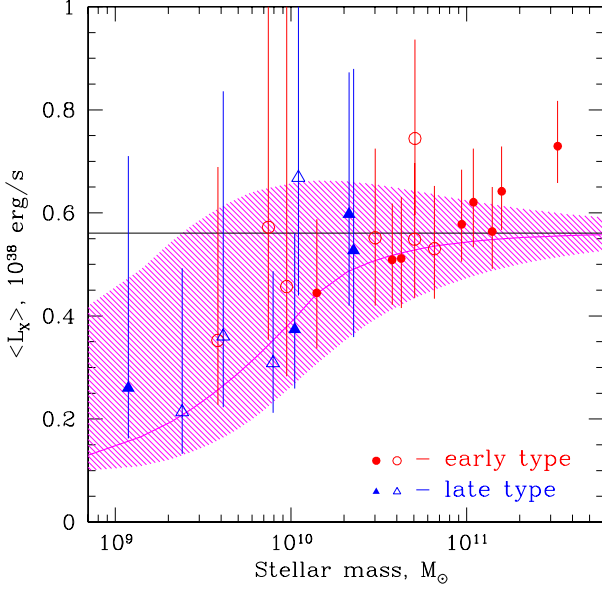


**Figure 17.** The average X-ray luminosity vs. stellar mass. The average luminosity,  $\langle L_X \rangle = L_{\text{tot}}/N_X$ , was computed for the sources with  $L_X > 10^{37}$  erg/s. The filled symbols are the data from Table 2, open symbols – smaller non-overlapping annuli in the same galaxies. Early and late type galaxies are shown by different symbols, as indicated in the legend. The thick solid line and the shaded area around it show the most probable value (section 2.5) of the average luminosity and its 67% uncertainty predicted from the average luminosity function. The horizontal line shows the value expected in the limit of large number of sources. The effects of statistics lead to smaller value of the average source luminosity for less massive (parts of) galaxies.

paper, the ratio of the total luminosities can be estimated:

$$\frac{L_{\text{LMXB}}}{L_{\text{HMXB}}} \sim 0.13 \frac{M_*/\text{SFR}}{10^{10} \text{ yrs}} \quad (12)$$

In the low SFR limit,  $\text{SFR} \lesssim 4 - 5 M_\odot/\text{yr}$ , the luminosity of high mass X-ray binaries will be subject to effects of statistics (section 2.5) and the ratio of the most probable values is given by:

$$\frac{L_{\text{LMXB}}}{L_{\text{HMXB}}} \sim 0.34 \frac{M_*/\text{SFR}}{10^{10} \text{ yrs}} \text{SFR}^{-2/3}, \quad \text{SFR} \lesssim 4.2 M_\odot/\text{yr} \quad (13)$$

The two above dependences intersect at  $\text{SFR} \approx 4.2 M_\odot/\text{yr}$ ,

The ratio of the number of sources depends non-monotonically on the threshold luminosity  $L_{\text{min}}$ . For the sources brighter than  $10^{38}$  erg/s it equals to:

$$\frac{N_{\text{LMXB}}}{N_{\text{HMXB}}} \sim 0.35 \frac{M_*/\text{SFR}}{10^{10} \text{ yrs}} \quad (14)$$

The coefficient in the above formula is 0.66, 0.37, 0.14 for  $L_{\text{min}} = 10^{37}, 10^{36}, 10^{35}$  erg/s respectively. Note, that the last number is based on extrapolation of the luminosity functions beyond the luminosity range covered by data.

### 6.5 Average luminosity of LMXBs

Given the shape of the LMXB XLF (Fig.13), the effects of statistics are not very pronounced in the considered range of

the stellar mass,  $\log(M_*) \sim 9 - 11.5$ , and do not affect significantly the  $L_X - M_*$  relation (thick solid line and shaded area around it in Fig.14). They are more noticeable when considering average luminosity of X-ray sources in a galaxy and lead to an artificial (unphysical) dependence of the average luminosity on the stellar mass (Fig.17). As illustrated by Fig.17, the observed dependence agrees well with the theoretical prediction based on the shape of the average XLF.

### 6.6 Bulge and disk populations in spiral galaxies

The deviation of X-ray growth curves from the distribution of the near-infrared light observed in the disks of spiral galaxies has been attributed in section 3.4 to the contribution of high mass X-ray binaries. In Fig.18 we further support this suggestion by comparing the X-ray luminosity functions of the bulge and disk population in M101. The observed difference in the number of sources and the shapes of their luminosity distributions agree both qualitatively and quantitatively with that expected from the “universal” luminosity functions of high and low mass X-ray binaries. Also shown in Fig.18 is the expected contribution of the low mass X-ray binaries in the disk of M101, predicted from its near-infrared luminosity and using the X-ray/NIR ratio derived for the bulge. The smallness of the expected number of LMXBs in the disk is in a good agreement with the fact, that outside the bulge of M101, the sources exhibit strong concentration towards the spiral arms, with the source density in the inter-arm regions being close to the density of background sources (Pence et al. 2001).

The disk of M101 has a rather small ratio of the stellar mass to the star formation rate,  $M_*/\text{SFR} \sim 2.4 \cdot 10^9$  yrs. Correspondingly (section 6.4), the LMXB contribution to the disk population of the compact X-ray sources is small and the luminosity function of the disk sources is close to that of HMXBs. In a general case, the population of the compact X-ray sources can be a superposition of the high and low mass X-ray binaries with comparable relative contributions, resulting to a complex shape of the luminosity distribution, coinciding neither with LMXB nor with HMXB XLF. This might explain a variety of the shapes of the luminosity functions observed by Chandra in different regions of nearby late type galaxies (e.g. Kong et al. 2003), as illustrated by right panel of Fig.18, showing the luminosity distribution in a large region of M81, including both bulge and disk population. Due to rather large value of the  $M_*/\text{SFR} \sim 4.6 \cdot 10^{10}$  yrs, comparable fractions of low and high mass X-ray binaries are expected. The total luminosity function of all sources can be presented as a sum of LMXB and HMXB contributions (Fig.18), in agreement with different luminosity distributions of the sources near the spiral arms and in the inter-arm regions observed by Chandra (Swartz et al. 2003).

### 6.7 Individual galaxies

The  $L_X$  growth curves of two galaxies, NGC1553 and NGC1291, show significant deviations from the distribution of the NIR light (Fig.4). The luminosity distributions for these two galaxies also exhibit largest deviations from the average XLF, although consistent with the latter within sta-

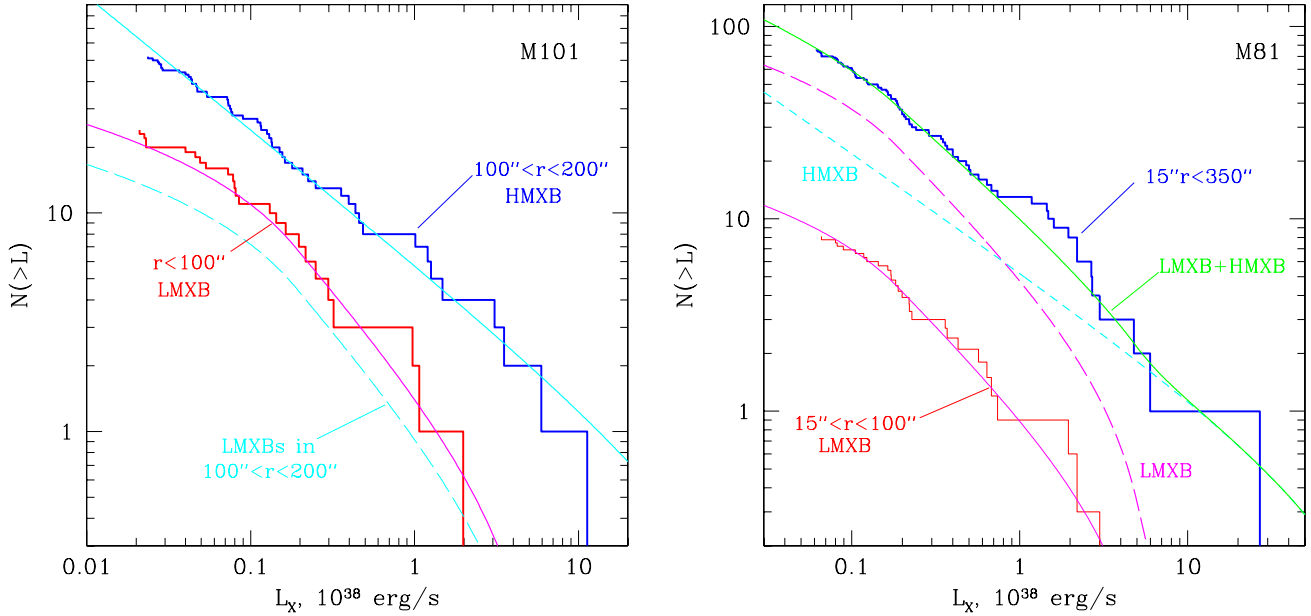


**Figure 18.** *Left:* XLF of bulge ( $r < 100''$ ) and disk ( $100'' < r < 200''$ ) of M101. The upper solid line shows predicted XLF of HMXBs corresponding to star formation rate of  $1.1 M_{\odot}/\text{year}$ , the lower solid line – predicted XLF of LMXBs with the normalization equal to the best fit value for M101 (e.g. Fig.11). The dashed line shows predicted contribution of the LMXBs to the disk population of X-ray binaries. It was computed using corresponding near-infrared luminosity and the same X-ray/NIR ratio as determined from the bulge population. *Right:* XLF of the inner bulge ( $15'' < r < 100''$ ) and bulge+disk ( $15'' < r < 350''$ ) populations in M81. The lower solid line is predicted XLF of LMXBs in the inner bulge, the short-dashed, long dashed and upper solid lines show contribution of HMXBs (SFR= $1 M_{\odot}/\text{yr}$ ) and LMXBs in the XLF of bulge+disk and their sum. In calculating the LMXB XLF for the bulge+disk the X/mass ratio of the bulge was multiplied by a factor of 0.75. The observed and predicted XLFs of the bulge are scaled down by a factor of 0.3 for clarity.

tistical uncertainties, according to the Kolmogorov-Smirnov test (Table 4).

These two galaxies might indeed present an example of the population age dependent variations in the shape of the luminosity distribution. In both cases the deviations from the average LMXB XLF occur at the high luminosity end as might be expected for such variations. Below we assess the statistical significance of the observed deviations and discuss alternative interpretations.

#### 6.7.1 NGC1553

Comparison of  $N_X$  and  $L_X$  growth curves for this S0 galaxy indicates possible variations of the luminosity distribution with the distance from the nucleus. This is confirmed by Fig.19, presenting luminosity functions for the inner and outer regions. In the inner ring, the luminosity distribution of the sources is consistent with that of other early type galaxies (solid smooth line marked “LMXB”). In the outer ring, on the contrary, it deviates significantly from the average (long-dashed line), both in the slope of the distribution and in the luminosity of the brightest sources. Although the luminosity function of all sources from  $15'' < r < 150''$  is consistent with the average LMXB XLF (Table 4), the outer ring taken separately gives the value of the Kolmogorov-Smirnov probability of  $\approx 2.1 \cdot 10^{-2}$ . In particular, 3 sources with  $L_X \gtrsim 10^{39}$  erg/s are observed at the radial distance  $50'' \lesssim r \lesssim 150''$  from the nucleus. Although their luminosities

are not extreme – still by a factor of  $\sim 10$  below that of the brightest ULXs in star forming galaxies, they nevertheless stand out in our sample. The nature of these sources is unclear. They do not coincide with any of the known globular clusters in the galaxy (Blanton et al. 2001). At the time of writing, there were no repeated observations of NGC1553, therefore their transient nature can not be established.

The shape of the XLF is reminiscent of that observed in the disks of the spiral galaxies (cf. Fig.18). Hypothetically it could be understood as a superposition of the LMXB and HMXB populations (solid line in Fig.19). However, such an explanation would require star formation on the level of  $\sim 1 - 2 M_{\odot}/\text{yr}$ . Although on-going star formation in NGC1553 can not be entirely excluded – it forms an interacting pair with NGC1549 (Bridges & Hanes 1990), the required value of SFR exceeds by an order of magnitude the star formation rates detected in some of the S0 galaxies (e.g. Pogge & Eskridge 1987). Moreover, the value of the far-infrared flux observed by IRAS,  $F_{60\mu} = 0.55$  and  $F_{100\mu} = 1.14$  Jy (NED, <http://nedwww.ipac.caltech.edu>), constrains the present star formation rate in NGC1553 by  $\lesssim 0.1 M_{\odot}/\text{yr}$ .

Another possibility is that the field of NGC1553 is contaminated by a fluctuation in the density of the CXB sources. An indirect evidence in favor of this interpretation is provided by the detection of another very bright source in the periphery of NGC1553 located at  $\approx 3.5'$  from the nucleus (the source no.38 in the Table 1 of Blanton et al. (2001)). Its

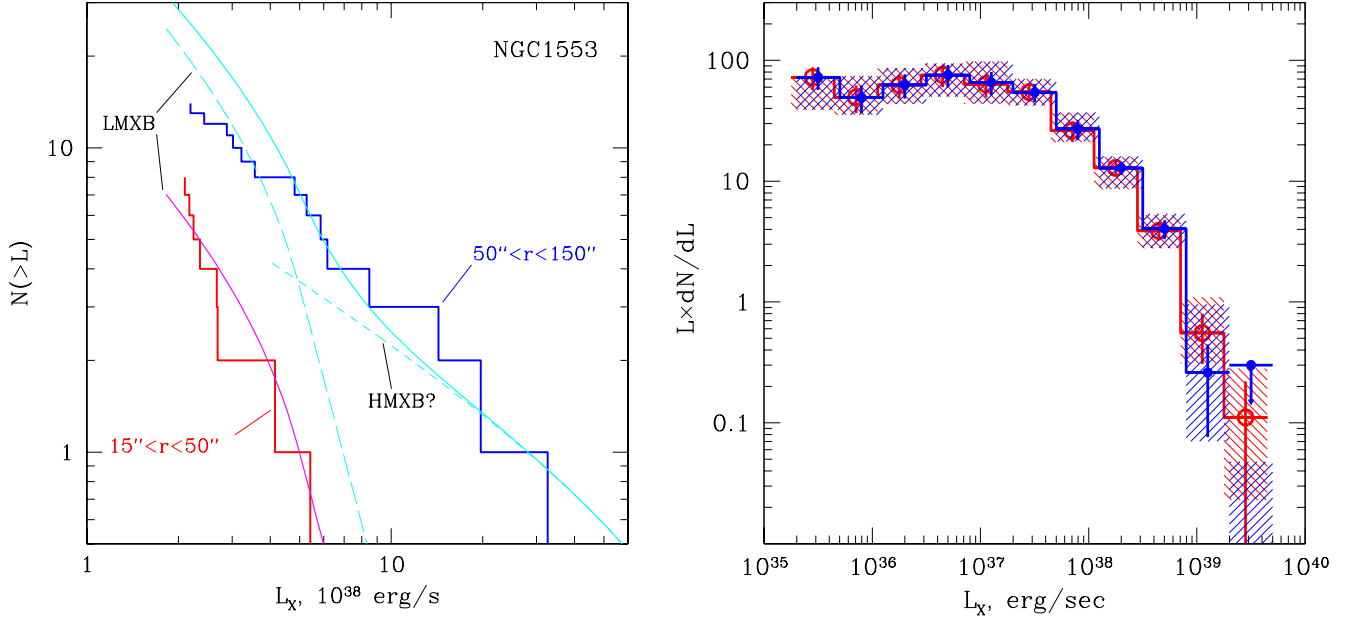


**Figure 19.** NGC1553: *Left:* XLFs in two annuli,  $15'' < r < 100''$  and  $50'' < r < 150''$ . The histograms show the observed distributions. The lower solid curve shows expected distribution of LMXBs with the normalization equals to the best fit value for the inner region. The dashed curve shows expected LMXB population for the outer region, its normalization was computed using respective near-infrared luminosity and the same X-ray/NIR ratio as determined for the inner region. The short-dashed curve shows luminosity distribution of the HMXBs expected for  $\text{SFR}=2 \text{ M}_\odot/\text{yr}$ , the solid line – the sum of LMXB and HMXB populations. *Right:* Effect of NGC1553 on the average LMXB XLF. Solid and grey open symbols show the average XLF computed without and with the NGC1553 sources. The upper limit is at 90% confidence. The shaded areas have the same meaning as in Fig.13. The two histograms are shifted horizontally with respect to each other by a small offset for clarity.

luminosity is  $L_X \sim 9.4 \cdot 10^{39} \text{ erg/s}$  assuming that it is a member of galactic population of the compact sources. An optical counterpart has been found in the DSS plate (Blanton et al. 2001). The blue magnitude, listed in the USNO-2 catalog,  $m_B = 20.4$ , would correspond to the luminosity  $L_B \sim 6 \cdot 10^6 L_\odot$  if the source was located at the distance of NGC1553. Obviously, this source is a background AGN (a foreground object in the Galaxy is excluded by the  $F_X/L_{\text{opt}} \sim 0.5$ ). As the expected number of such bright background objects is  $N_{\text{CXB}} \sim 0.08$ , its presence might indicate an enhancement in the number density of CXB sources in the field of NGC1553. Detection of optical counterparts of other apparently luminous sources would prove this hypothesis, however optical observations inside  $\sim 1 - 2$  effective radii of the galaxy are complicated by its optical emission. Note, that in order to account for the number of bright sources observed in the outer ring (Fig.19), a significant over-density of the CXB sources, by a factor of  $\sim 2 - 3$ , on arcmin angular scale is required, which is probably too large to be explained in terms of the average angular correlation function of CXB sources (Vikhlinin & Forman 1995).

In conclusion, we note, that although NGC1553 clearly stands out in our sample from the point of view of the  $L_X$  growth curve and the shape of the luminosity function, its growth curve for the number of sources and  $X/M_*$  ratios are within the dispersion of the values observed in other nearby galaxies (Table 2, Figs.3, 14, 15). We give in Table 2 the X-ray and near-infrared parameters for both the inner ring and the entire  $15'' < r < 150''$  region. NGC1553 data were

not included in constructing the average luminosity function (Fig.13) and determination of its best fit parameters (Table 3). Its influence on the shape of the average luminosity function is illustrated in the right panel in Fig.19, showing that associated changes are well within the statistical and systematic uncertainties.

#### 6.7.2 NGC1291

The deviations of the  $L_X$  growth curve from the NIR profile are significantly less pronounced and are within about  $\lesssim 2\sigma$ . The examination of the luminosity distribution in different annuli did not reveal any peculiarities, similar to those observed in NGC1553. The overall luminosity distribution (Fig.12) agrees very well with the average LMXB XLF at low luminosities,  $L_X \lesssim 2.5 \cdot 10^{38} \text{ erg/s}$ , but appears to have a too abrupt cut-off above this value. To characterize it quantitatively, we note that the average XLF, normalized to the total number of sources at the adopted completeness limit,  $3 \cdot 10^{37} \text{ erg/s}$ , predicts  $\approx 2.7$  sources above the luminosity of the brightest observed source,  $2.6 \cdot 10^{38} \text{ erg/s}$ . For a Poisson distribution with expectation value of 2.7, the probability to draw zero is 6.7%, i.e. the case of NGC1291 presents  $\lesssim 2\sigma$  deviation. This value of probability is not small enough to claim presence of statistically significant deviations from the average XLF.

### 6.8 The Milky Way

The luminosity function of LMXB sources in the Milky Way and X-ray/ $M_*$  ratios are by a factor of  $\sim 1.5 - 2$  lower than the main group of galaxies on all plots (Fig. 8, 14, 15). As the X-ray/ $M_*$  ratios for the Milky Way were derived in a different way than for other galaxies, they are subject to different systematic uncertainties. We discuss below various factors, affecting its X-ray/NIR ratios.

The stellar mass of the Milky Way was estimated using the K-band growth curve and mass-to-light ratio of M31, which is sufficiently similar to our Galaxy in the morphological type. In the growth curve analysis we used the low mass X-ray binaries located at  $X > 0$ , where the origin of the Cartesian coordinate system is located at the Galactic Center and the X-axis is directed towards the Sun (Grimm et al. 2002). Thus, to the accuracy defined by the completeness of the LMXB catalog, our analysis should include  $\sim 1/2$  of the Galaxy. Correspondingly, the NIR growth curve of M31 was scaled down by a factor of 2, resulting in the K-band luminosity of the half of the Galaxy  $L_K \approx 4.5 \cdot 10^{10} L_\odot$  (calculated from the best fit total K-band magnitude of M31,  $m_{tot} = 0.5$ , Table 1). This value is consistent with accuracy better than  $\lesssim 10\%$  with that expected from the total K-band luminosity of the Milky Way,  $L_{MW,K} \approx 9.6 \cdot 10^{10} L_\odot$ , obtained from 3D modeling of the DIRBE data (Malhotra et al. 1996). The K-band mass-to-light ratio obtained from the optical color of M31 is  $M_*/L_K \approx 0.68$ . This value is close, but not identical to the value obtained by Thronson & Greenhouse (1988) for the solar neighborhood,  $M_*/L_K \approx 0.78$ . It should be mentioned, though, that the latter value was derived for the disk population of the Galaxy and might not be appropriate for the older stellar population of the bulge. Note, that higher mass-to-light ratio would increase the stellar mass estimate, decrease of the X-ray/mass ratio, and therefore would result in a larger discrepancy between the Milky Way and other galaxies.

An important factor is the completeness of the LMXBs catalog. Grimm et al. (2002) used the sources with known distances and reliable optical identification. Comparing with the stellar mass distribution in the Galaxy, they concluded, that their sample is reasonably complete above  $\sim 10^{36}$  erg/s and within  $\sim 10 - 12$  kpc from the Sun. In computing the final luminosity function and total X-ray luminosity of the Galaxy they introduced luminosity dependent volume correction using the mass model of the Galaxy. On the other hand we computed the X-ray/NIR ratios using the sources located at  $X > 0$  in the range of projected galactocentric distances  $1 \text{ kpc} < R_{proj} < 10 \text{ kpc}$ , which, strictly speaking, is not identical to the definition of the completeness region in Grimm et al. (2002). It is not clear, whether this procedure could result in an underestimate of the Milky Way luminosity by a factor of  $\sim 1.5 - 2$ . On the other hand, the value of the X-ray-to-mass ratio, derived in this paper,  $L_X/M_* \approx 3.5 \cdot 10^{28} \text{ erg/s}/M_*$  is close but somewhat lower than the one obtained by Grimm et al. (2002), using different method,  $L_X/M_* \approx 5 \cdot 10^{28} \text{ erg/s}/M_*$ .

Finally, Grimm et al. (2002) used the source luminosities averaged over 5 year period of the ASM/RXTE observations. Depending on the properties of the collective X-ray light curve of the Galaxy this might lead to a difference be-

tween their average value and the value to be most probably observed in a snapshot.

### 6.9 Total energy output of LMXBs and HMXBs

The calibration of the  $L_X$ -SFR and  $L_X - M_*$  relations obtained by Grimm et al. (2003) and in the present paper allows us to estimate the total energy output of X-ray binaries throughout the life time of a galaxy.

The total energy output of HMXBs in the Chandra passband can be estimated as:

$$E_{\text{HMXB}} = \int \frac{L_X}{\text{SFR}} \text{SFR}(t) dt = \frac{L_X}{\text{SFR}} \alpha \eta M_* \quad (15)$$

where  $\text{SFR}(t)$  is the time dependent star formation rate of stars more massive than  $5 M_\odot$  and describes the star formation history of the galaxy,  $M_*$  – its present stellar mass,  $\alpha$  – fraction of the total mass of stars formed during the life time of the galaxy, which presently resides in stars (of all masses),  $\eta$  is the IMF-dependent mass fraction of stars more massive than  $5 M_\odot$  and accounts for the fact, that  $L_X$ -SFR was calibrated for formation rate of stars  $M > 5 M_\odot$ :

$$\eta = \frac{\int_{5M_\odot}^{M_{\text{max}}} \xi(M) M dM}{\int_{M_{\text{min}}}^{M_{\text{max}}} \xi(M) M dM} \quad (16)$$

For the “extended” Miller-Scalo IMF (Kennicutt 1983),  $\xi(M) = M^{-1.4}$  for  $0.1 M_\odot \leq M \leq 1 M_\odot$ , and  $\xi(M) = M^{-2.5}$  for  $1 M_\odot \leq M \leq 100 M_\odot$ ,  $\eta \approx 0.23$ .

Studying the intermediate redshift (up to  $z \approx 1.3$ ) starburst galaxies observed by CHANDRA in the Hubble Deep Field North Grimm et al. (2003) showed that the calibration of the  $L_X/\text{SFR}$  ratio based on the local galaxies is valid for these distant galaxies as well. For this reason the  $L_X/\text{SFR}$  ratio can be taken outside the integration in eq.(15) With  $L_X/\text{SFR} \approx 6.7 \cdot 10^{39} \text{ erg/s per } M_\odot/\text{yr}$  and assuming  $\alpha \sim 0.3 - 0.5$ , the total energy output of HMXBs is

$$E_{\text{HMXB}} \approx 2.4 \cdot 10^{57} \left( \frac{\alpha}{0.5} \right) \left( \frac{M_*}{10^{11} M_\odot} \right) \text{ erg} \quad (17)$$

The energy output of LMXBs is:

$$E_{\text{LMXB}} = \int \frac{L_X}{M_*}(t) M_*(t) dt \sim \frac{L_X}{M_*} M_* t_{\text{gal}} \quad (18)$$

Unlike for high mass X-ray binaries, eq.(15), the  $L_X$ -mass relations was measured for nearby galaxies only. Therefore the last equality in the above equation relies on the extrapolation of this relation to high redshifts. As the evolution effects might play an important role in the case of LMXBs, this estimate is significantly less robust than that for HMXBs. However, the details of the evolution of the luminosity distribution of LMXBs are yet unexplored, and even a crude estimate might be of certain interest. Using  $L_X/M_* \approx 8 \cdot 10^{39} \text{ erg/s per } 10^{11} M_\odot$  and assuming  $t_{\text{gal}} \sim 10^{10} \text{ yrs}$ :

$$E_{\text{LMXB}} \sim 2.5 \cdot 10^{57} \left( \frac{M_*}{10^{11} M_\odot} \right) \left( \frac{t_{\text{gal}}}{10^{10} \text{ yrs}} \right) \text{ erg} \quad (19)$$

which is close to the value obtained for HMXBs. As low mass X-ray binaries were brighter in the past, this number is a lower limit on their energy output in the Chandra passband.

## 6.10 Clusters of galaxies

For the typical value of the stellar mass in the rich clusters of galaxies,  $M_* \sim 10^{13-14} M_\odot$ , the expected X-ray luminosity of low mass X-ray binaries is  $L_{\text{LMXB}} \sim 10^{42-43}$  erg/s. Taken at face value, this is a negligible fraction, at the level of  $\lesssim$  few per cent, of the luminosity of the X-ray emitting gas,  $L_{\text{gas}} \sim 10^{43-45}$  erg/s.

However, due to different energy spectra of X-ray gas and of X-ray binaries, contribution of the latter might become significant in certain energy ranges. It is well known that the hard tails of Comptonized radiation might be present in the spectra of X-ray binaries. Depending on the spectral state, the spectrum of the Comptonized component extends to  $\sim 100 - 200$  keV (low state) or to the  $\sim$  MeV energies in the high state of black hole binaries. Importantly, in the low state, the hard spectral component is observed in the spectra of both black hole and neutron star binaries (e.g. Sunyaev et al. 1991; Gilfanov et al. 1998). The hard X-ray spectral component might amplify the relative contribution of X-ray binaries at high X-ray energies,  $\sim 20 - 150$  keV and higher. An accurate calculation of this contribution would require knowledge of the X-ray binaries luminosity distribution in hard X-rays, far beyond the Chandra bandpass. For a crude, an order of magnitude estimate we note, that in the low spectral state, corresponding to the luminosities below  $\sim (2 - 3) \cdot 10^{37}$  erg/s, the luminosity above  $\sim 30$  keV is at the very least equal to that emitted in the Chandra bandpass. Given the shape of the LMXB luminosity function, the sources with  $L_X \lesssim (2 - 3) \cdot 10^{37}$  erg/s contribute  $\sim 25\%$  to the combined X-ray luminosity of LMXBs. Thus, only due to X-ray binaries in the low spectral state the luminosity above  $\sim 20$  keV should be of the order of  $\sim 10^{42-43} \times 0.25 \sim \text{few} \times 10^{41-42}$  erg/s. This is, obviously, a lower limit to the actual value of the total hard X-ray luminosity due to LMXBs. On the other hand, for typical temperatures of the X-ray gas in the clusters of galaxies,  $T_{\text{gas}} \sim 5$  keV, of the order of  $\lesssim 10^{-2}$  of the total luminosity is emitted above  $\sim 20$  keV, i.e.  $\lesssim 10^{41-43}$  erg/s which is comparable to the lower limit on the luminosity of LMXBs. At higher energies the situation becomes even more favorable for LMXBs. As the emissivity of X-ray gas falls off with radius quicker, than the number density of the galaxies, the relative contribution of LMXBs in hard X-ray energy domain will be further enhanced in the outer parts of the clusters. We should note, however, that the hard X-ray emission may be dominated by the low luminosity AGNs, depending on their actual frequency and the luminosity distribution.

## 7 SUMMARY

We analyzed population properties of compact X-ray sources in nearby external galaxies of various morphological types and of the LMXB sources in the Milky Way. We focused our analysis on the old stellar systems – early type galaxies and the bulges of spiral galaxies. This ensures that the compact X-ray sources in the external galaxies are dominated by low mass X-ray binaries. In the case of the Milky Way we explicitly selected LMXB sources based on the results of Grimm et al. (2002). Our findings can be summarized as follows.

- (i) For all galaxies the azimuthally averaged spatial distri-

bution of the number of LMXBs follows closely the distribution of the near-infrared light (Fig.3). Our analysis covered the central parts of the galaxies, out to  $\sim 1.5 - 2$  effective radii in early type galaxies and  $\sim$ inside the inner bulge in spiral galaxies. With the exception of NGC1553 and, to lesser extend, NGC1291 (section 6.7), the same is true for the distribution of their combined luminosity in the Chandra bandpass,  $\sim 0.5 - 8$  keV (Fig.4).

In the disks of spiral galaxies, on the contrary, the distribution of the number and combined luminosity of the compact sources deviates significantly from the NIR profile. The deviation is caused by the contribution of HMXBs, as evidenced by the example of the Milky Way (Fig.5) and by the comparison of the luminosity functions of the disk and bulge in M101 and M81 (Fig.18).

- (ii) Considering galaxies as whole, the total number of LMXBs and their collective luminosity are directly proportional to the stellar mass of the host galaxy (Fig.14), the latter calculated from the K-band luminosity using color-based correction of the mass-to-light ratio (eq.(2)).

There is statistically significant dispersion between values of  $X/M_*$  ratios, with the fractional rms of  $\sim 25\%$  and  $\sim 40\%$  for  $L_X/M_*$  and  $N_X/M_*$  respectively (Fig.15). The accuracy of the color-based correction of the K-band mass-to-light ratio in the present analysis is insufficient to establish reality of the observed dispersion. Neither it is sufficient to confirm or rule out the possibility of a morphological type-dependent trend in the  $X/M_*$  ratios. If present, its effect does not exceed a factor of  $\sim 1.5 - 2$  (Fig.15).

On average, the number of sources with  $L_X > 10^{37}$  erg/s and their combined luminosity are related to the stellar mass as follows:

$$\begin{aligned} N_X(> 10^{37} \text{ erg/s}) &= 142.9 \pm 8.4 \text{ sources per } 10^{11} M_\odot \\ L_X(> 10^{37} \text{ erg/s}) &= (8.0 \pm 0.5) \cdot 10^{39} \text{ erg/s per } 10^{11} M_\odot \end{aligned} \quad (20)$$

The precise values of the coefficients in these formulae depends somewhat on the weighting method (section 5).

- (iii) The X-ray/ $L_{\text{NIR}}$  ratios show clear dependence on the morphological type (Fig.16). The average values are:

$$\begin{aligned} N_X(> 10^{37} \text{ erg/s}) &= (81 - 135) \text{ sources per } 10^{11} L_\odot \\ L_X(> 10^{37} \text{ erg/s}) &= (3.3 - 7.5) \cdot 10^{39} \text{ erg/s per } 10^{11} L_\odot \end{aligned} \quad (21)$$

where the first and the second number in the parenthesis correspond to average values for late and early type galaxies respectively. The average values for all galaxies are  $117 \pm 12.4$  sources and  $(6.1 \pm 0.5) \cdot 10^{39}$  erg/s for  $N_X$  and  $L_X$  respectively. These numbers obviously depend on the content of our sample.

Even stronger dependence on the morphological type should be observed at shorter wavelength, e.g. in the B-band, often used to characterize relation between X-ray and optical properties of the galaxies.

- (iv) The shape of the luminosity function of the LMXBs is similar in different galaxies (Fig.8, 9, 10). The data on individual galaxies, with a possible exception of NGC1553 (section 6.7), are broadly consistent with the average luminosity function of LMXBs, derived using all galaxies from our sample (Fig.12, Table 3, 4). The average LMXBs XLF has a complex shape and differs significantly from that of HMXBs (Fig.13, Table 3). It is consistent with a power law with differential slope of  $\approx 1$  at low luminosities, gradually steepens

above  $\log(L_X) \sim 37.0 - 37.5$  and has a rather abrupt cut-off at  $\log(L_X) \sim 39.0 - 39.5$ . In the  $\log(L_X) \sim 37.5 - 38.7$  luminosity range it is approximately represented by a power law with differential slope of  $\sim 1.7 - 2.0$ . The normalization of the luminosity function found in individual galaxies is proportional to the stellar mass (Fig.11).

(v) The luminosity of the brightest sources in our sample of old stellar systems (with total stellar mass of  $\sim 10^{12} M_\odot$ ) does not exceed the value of  $L_X \sim (2 - 3) \cdot 10^{39}$  erg/s. The maximum luminosity of HMXB sources is by a factor of  $\sim 10$  larger. This can be used to diagnose on-going star formation.

(vi) Relative contributions of low and high mass X-ray binaries to the population of compact sources in a galaxy is defined by the ratio of its stellar mass to the present value of star formation rate, according to the formulae given in section 6.4.

(vii) Calibration of the  $L_X - M_*$  relation derived in the present paper allows one to use the X-ray luminosity of a galaxy due to low mass X-ray binaries as an independent stellar mass indicator. Applicability of this calibration to distant galaxies at larger redshifts is yet to be established and might require proper account for the X-ray binary evolution effects.

(viii) The total energy outputs of LMXBs and HMXBs in the Chandra passband during the life time of a galaxy are of the same order,  $\sim \text{few} \times 10^{57} \times (M_*/10^{11} M_\odot)$  erg. In the case of LMXBs, this number does not take in to account the binary evolution effects and, most likely, is a lower limit.

## REFERENCES

- Bell E. & de Jong R., 2001, ApJ, 550, 212  
 Blanton E., Sarazin C. & Irwin J., 2001, ApJ, 552, 106  
 Bridges T. & Hanes D., 1990, AJ, 99, 1100  
 Brinchmann J. & Ellis R., 2000, ApJ, 536, L77  
 David L., Jones C. & Forman W., 1992, ApJ, 388, 82  
 de Vaucouleurs G. & Corwin H.G., 1977, ApJS, 33, 219  
 de Vaucouleurs G. et al., 1991, Third Reference Catalog of Bright Galaxies. Springer-Verlag (RC3)  
 Fabbiano G. & White N., 2003, in: "Compact Stellar X-ray Sources", Cambridge University Press (eds., W. Lewin & M. van der Klis), astro-ph/0307077  
 Finoguenov A. & Jones C. 2002, ApJ, 574, 754  
 Fioc M. & Rocca-Volmerange B., 1999, A&A, 351, 869  
 Fitzpatrick L., 1999, PASP, 111, 63  
 Gehrels N. 1986, ApJ, 303, 336  
 Gezari D.Y., Pitts P.S. & Schmitz M., 1999, "Catalog of Infrared Observations, Edition 5"  
 Ghosh P. & White N., 2001, ApJ, 559, L97  
 Gilfanov M. et al., 1998, A&A, 338, L83  
 Gilfanov M., Grimm H.-J. & Sunyaev R., 2003, in preparation  
 Griffiths R. & Padovani P., 1990, ApJ, 360, 483  
 Grimm H.-J., Gilfanov M. & Sunyaev R., 2002, A&A, 391, 923  
 Grimm H.-J., Gilfanov M. & Sunyaev R., 2003, MNRAS, 339, 793  
 Irwin J.A., Sarazin C.L. & Bregman J.N., 2003, ApJ, 570, 152  
 Jensen J., et al., 2003, ApJ, 583, 712  
 Kauffmann G. et al., 2003, MNRAS, 341, 33  
 Kennicutt R., 1983, ApJ, 272, 54  
 Kim D.-W. & Fabbiano G., 2003, ApJ, 586, 826  
 Kong A. et al., 2002, ApJ, 577, 738  
 Kong A. et al., 2003, ApJ, 585, 298  
 Kraft R.P. et al., 2001, ApJ, 560, 675  
 Maccarone T.J., Kundu A. & Zepf S.E., 1996, ApJ, 586, 814  
 Malhotra S. et al., 1996, ApJ, 473, 687  
 Manners J.C. et al., 2003, MNRAS in press, astro-ph/0207622  
 Mendez R., 2001, ApJ, 563, 135  
 Morton D.C., Andereck C.D. & Bernard D.A., 1977, ApJ, 212, 13  
 Okamura S., Kanazawa T., Kodaira K., 1976, PASJ, 28, 329  
 Pahre M.A., 1999, ApJSS, 124, 127  
 Pence et al., 2001, ApJ, 561, 189  
 Pfahl E.D., Rappaport S. & Podsiadlowski Ph., 2003, ApJ, 597, 1036  
 Piro A. & Bildsten L., 2002, ApJ, 571, L103  
 Podsiadlowski Ph., Rappaport S. & Pfahl E.D., 2002, ApJ, 565, 1107  
 Pogge R. & Eskridge P., 1987, AJ, 92, 291  
 Postnov K., 2003, Ast.Lett., 29, 372  
 Prugniel Ph. & Heraudeau Ph., 198, A&AS, 128, 299 (HyperLeda)  
 Reichen M. et al., 1994, A&AS, 106, 523  
 Rosati P. et al., 2002, ApJ, 566, 667  
 Sarazin C.L., Irwin J.A. & Bregman J.N., 2001, ApJ, 556, 533  
 Sunyaev R. et al., A&A, 247, L29  
 Swartz D. et al., 2003, ApJSS, 144, 213  
 Trinchieri G. & Goudfrooij P., 2002, A&A, 386, 472  
 Thronson H. & Greenhouse M., 1988, ApJ, 327, 671  
 Verbunt F. & van den Heuvel E.P.J., 1995, in: X-ray Binaries, Eds: W.Lewin, J.van Paradijs & E.van den Heuvel, Cambridge Univ.Press, p.457  
 Vikhlinin A. & Forman W., 1995, ApJ, 455, L109